

NeuroVolve: Evolving Visual Stimuli toward Programmable Neural Objectives

Haomiao Chen^{1,2,3*}, Keith W Jamison^{1,3}, Mert R. Sabuncu^{1,2,3}, Amy Kuceyeski^{1,3}

¹Cornell University ²Cornell Tech ³Weill Cornell Medicine



Figure 1. **Images generated using NeuroVolve.** We visualize image trajectories optimized to activate specific brain regions. Starting from random seeds, NeuroVolve reveals region-selective features over iterations—recovering known high-level selectivity (e.g., FFA, PPA, EBA) and capturing low level sfeatures selectivity in early areas (e.g., V1, V2). It also supports compositional objectives, generating coherent images under complex multi-region constraints.

Abstract

What visual information is encoded in individual brain regions—and how do distributed patterns combine to create their neural representations? Prior work has used generative models to replicate known category selectivity in isolated regions (e.g., faces in FFA), but these approaches offer limited insight into how regions interact during complex, naturalistic vision. We introduce *NeuroVolve*, a generative framework that provides brain-guided image synthesis via optimization of a neural objective function in the embedding space of a pretrained vision-language model. Images are generated under the guidance of a programmable neural objective, i.e. activating/deactivating single regions or multiple regions together. *NeuroVolve* is validated by recovering known selectivity for individual brain regions,

while expanding to synthesize coherent scenes that satisfy complex, multi-region constraints. By tracking optimization steps, it reveals semantic trajectories through embedding space—unifying brain-guided image editing and preferred stimulus generation in a single process. We show that *NeuroVolve* can generate both low-level and semantic feature-specific stimuli for single ROIs, as well as stimuli aligned to curated neural objectives. These include co-activation and decorrelation between regions, exposing cooperative and antagonistic tuning relationships. Notably, the framework captures subject-specific preferences, supporting personalized brain-driven synthesis and offering interpretable constraints for mapping, analyzing, and probing neural representations of visual information.

1. Introduction

Much is known about how the human visual cortex processes information, particularly its regional specialization and selectivity. Early visual areas respond to low-level features such as orientation, texture, and motion [5, 13], while higher-order areas are selectively activated by semantically meaningful categories such as faces, places, words or food [7, 9, 10, 15–18, 29]. However, these findings typically emerge from hypothesis-driven experiments using small, predefined sets of stimuli. This limits discovery, especially regarding how the brain encodes rich, real-world scenes involving multiple objects and concepts simultaneously. In particular, such approaches rarely capture how multiple regions cooperate or compete during naturalistic perception.

Recent work has leveraged generative models to study neural selectivity in a data-driven manner [3, 11, 21, 22, 28]. Some methods optimize latent codes of GANs [8] or diffusion models [12, 30] to synthesize brain-aligned images [11, 21, 28]. While effective, these methods rely on image-space gradients are very inefficient, limiting scalability. Other approaches [3, 22] derive fixed embeddings that maximize or suppress activity in a single region and condition generation on those. However, these methods are limited to simple objectives (e.g., maximizing or suppressing a single region or voxel) and lack flexibility for more expressive or compositional neural goals.

NeuroVolve addresses these limitations by introducing an optimization-based framework for brain-guided image synthesis under *programmable neural objectives*, operating directly in a semantic embedding space. It enables the use of contrastive vision-language models and diffusion models to uncover functional specialization as well as more complex neural patterns, such as multi-region co-activation in a flexible and data-driven manner. Built on the rich embedding space of a contrastive vision-language model [20], NeuroVolve reformulates brain-constrained image generation as an optimization problem: navigating the landscape defined by a voxelwise encoding model and a target neural objective to actively find the embedding that best satisfies a desired brain activation pattern (Fig. 2b).

In contrast to prior methods [3, 22] that rely on fixed embeddings derived from encoder weights, NeuroVolve performs brain guided iterative optimization—yielding a **semantic trajectory** of intermediate embeddings that reflect stepwise alignment with the neural objective. These embeddings are then used to condition a frozen diffusion model for image generation. This trajectory unifies brain-guided image editing (early steps) and preferred stimulus synthesis (final states), while revealing interpretable visual transitions shaped by neural constraints. Because optimization occurs in a pretrained, semantically structured embedding space, the process is both efficient and expressive, producing high-quality, meaningful images. Analysis of these tra-

jectories enables data-driven exploration of visual cortical representations, including under complex, multi-objective conditions. Critically, because the optimization is guided by subject-specific encoding models, NeuroVolve also captures individual variability in neural selectivity—opening new directions for personalized stimulus design, brain modulation, and neuroscience applications.

Contributions We make the following contributions:

- **A novel embedding-space optimization framework** for brain-guided image synthesis, leveraging the semantic space of a pretrained vision-language model to efficiently explore and satisfy programmable neural objectives.
- **Support for programmable neural objectives** at both regional and voxel levels, enabling flexible goals such as activating individual regions, co-activating multiple regions, and suppressing specific voxels. By combining such objectives, our method facilitates fine-grained, data-driven exploration of cortical organization beyond traditional single-region maximization.
- **A unified image editing and synthesis approach**, where iterative optimization yields a semantic trajectory that reveals interpretable visual transitions under neural guidance.
- **Subject-specific image generation and tuning analysis**, demonstrating the capacity to capture individual differences in neural selectivity and generate personalized, brain-aligned stimuli.

2. Related works

Brain Mapping of Visual Representations A long tradition in visual neuroscience has characterized brain representations across the visual hierarchy, from low-level selectivity in early visual cortex (e.g., orientation, motion, spatial frequency) to high-level categorical selectivity for faces, places, bodies, words, and other semantic classes [5, 7, 10, 13, 16–18, 23, 25]. Many of these discoveries rely on carefully handcrafted stimuli specifically designed to activate targeted regions. Recent progress in neural encoding models that predict fMRI response from stimulus features and have enabled data-driven computational tests of brain selectivity in vision. [4, 6, 14, 24, 32, 33]. Our proposed method incooperates an image-compyable encoding model inline with this past work.

Diffusion Models The recent process in deep generative models has enabled sampling from complex high dimensional distribution. Diffusion models [12, 30] treat the data generation process as iterative noise removal, progressively refining random noise $x_T \sim \mathcal{N}(0, 1)$ into structured data $x_{T-1}, \dots, x_{t+1}, x_t, x_{t-1}, \dots, x_0$ through a trained denoising network. It is possible to condition the model on cat-

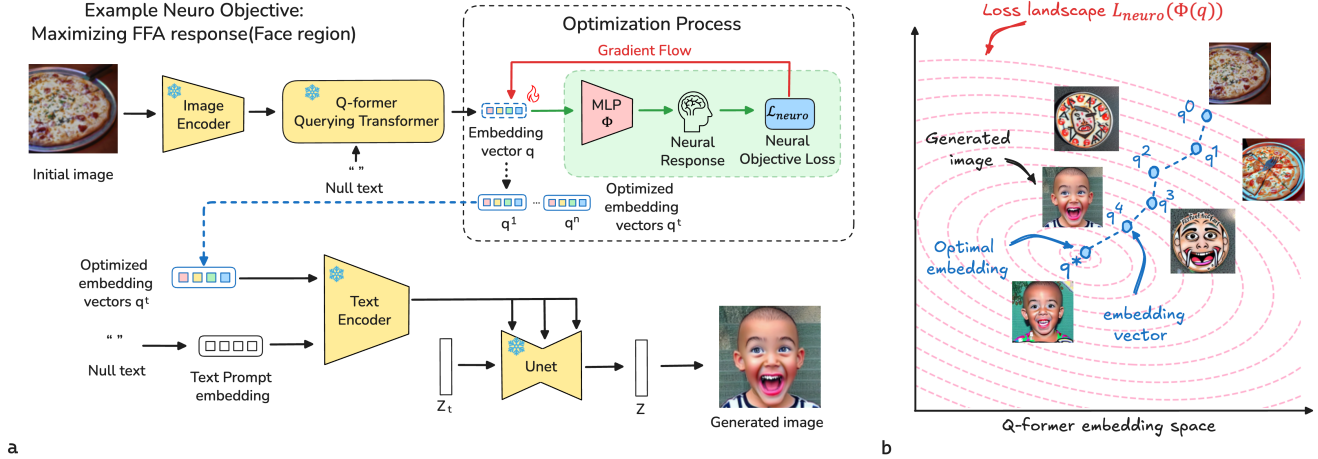


Figure 2. **Overview of the NeuroVolve framework.** (a) Starting from an initial image, we extract Q-Former embeddings using a frozen BLIP-2 encoder. These embeddings are then iteratively optimized under a neural objective using gradients from a learned subject-specific MLP Φ , which maps Q-Former embeddings to voxel-wise brain activity. The resulting embedding trajectory is used to guide a diffusion model (BLIP-Diffusion) for image synthesis. (b) Visualization of optimization in the Q-Former embedding space. NeuroVolve minimizes a neural objective loss to evolve the embedding toward a region-selective optimum (e.g., maximizing FFA). The resulting semantic trajectory produces interpretable, brain-aligned images.

egory, text or images. BLIP-diffusion [19] allows the diffusion process to be conditioned on vector in the semantic rich vision-language pretrained embedding space. Our paper employs BLIP-diffusion to synthesize images conditioned on Q-former embeddings.

Brain-Conditioned Image Generation Early work in brain-guided image synthesis used gradients from deep encoding models to reconstruct or generate images from neural activity in animals and humans [2, 26, 31], but often produced low-quality outputs. Later methods combined encoding models with generative networks to produce more naturalistic stimuli aligned with category-selective brain regions [3, 11, 21, 28]. For instance, [11, 28] used BigGAN, but were limited by ImageNet label constraints, reducing diversity. More recent approaches like BrainDive [21] employed diffusion models and backpropagated gradients from encoding models into the noise space. While visually effective, this process remains computationally expensive, as it requires optimization in the image space during generation. In contrast, NeuroVolve optimizes directly in the pre-trained Q-Former embedding space—improving efficiency, interpretability, and semantic control. Rather than updating latent noise vectors, we optimize the embedding that conditions the diffusion model, producing coherent, brain-aligned images via programmable neural objectives. Recent work like [3] and [22] generate images using CLIP-based embeddings, but are limited to fixed maximization or suppression vectors, reducing flexibility.

NeuroVolve unifies and extends both lines of work,

enabling iterative embedding optimization under flexible neural objectives—including co-activation and suppression—while revealing subject-specific tuning and semantic trajectories aligned with brain responses.

3. Methods

Our goal is to synthesize images that satisfy a desired *neural objective*—such as activating or suppressing single or multiple brain regions’ responses. We formulate this as a two-stage process: (1) optimization in a semantic embedding space guided by neural constraints, and (2) image synthesis conditioned on the optimized embeddings (Fig. 2).

In the first stage, we begin with either a random vector or a reference image and encode it into the embedding space of a pretrained vision-language model [20]. This embedding serves as the starting point for optimization. We then **iteratively update the embedding** to minimize a task-specific neural objective, using a trained voxel-wise fMRI encoder to define a differentiable loss landscape over the embedding space. This loss reflects the discrepancy between the predicted brain response and the target neural pattern. The resulting optimization trajectory consists of intermediate embeddings that increasingly align with the neural objective. In the second stage, we use these embeddings to condition a pretrained diffusion model [19], producing a *semantic image trajectory* that visualizes how the image content evolves under neural guidance. Early iterations yield subtle, interpretable changes from the initial image, while later stages converge toward stimuli predicted to optimally satisfy the neural objective. This two-stage framework enables flexi-

ble, programmable, and interpretable brain-aligned image synthesis.

We describe our approach in three parts: First, we introduce the voxel-wise neural encoding model that maps images to predicted brain responses. Next, we describe how we use this model to define neural objectives and optimize in the embedding space. Finally, we explain how optimized embeddings condition the diffusion process, yielding a visual trajectory that reveals semantic transformations under neural objectives.

3.1. Voxelwise neural encoding model

We train a voxel-wise brain encoding model F_θ to predict fMRI activation patterns from image inputs. Given an image $M \in \mathbb{R}^{3 \times H \times W}$ and its corresponding voxel-level response vector $r \in \mathbb{R}^N$, the encoder learns a mapping from image to brain activation: $F_\theta(M) = r$.

Building on recent findings that vision-language model embeddings provide strong representations for predicting neural responses [4, 32], we adopt a two-stage architecture. The first component is a frozen pretrained backbone from BLIP-2 [20], consisting of: a vision encoder to extract visual features, and a multimodal encoder Q-former for aligning image and text representations. We input an Null prompt “ ” as the text prompt to extract the overall scene-level embedding, avoiding bias toward any specific object in the image. Let q denote the embedding output from the Q-Former. Q-former produces a token embedding $q \in \mathbb{R}^{16 \times 768}$.

The second component is a voxel-wise prediction module Φ , implemented as a multilayer perceptron (MLP), which maps the Q-former embedding to predicted brain responses:

$$F_\theta(M) = \Phi(\text{Q-former}(M)) = \Phi(q_M) = r, r \in \mathbb{R}^N \quad (1)$$

We train the full model using mean squared error (MSE) loss between predicted and measured voxel responses. Evaluation on held-out test data shows that the model achieves high accuracy in predicting brain activity, demonstrating the utility of high-capacity multimodal embeddings for voxel-wise encoding. Implementation details and evaluation are included in the appendix.

3.2. Optimization in Embedding Space

Then our goal is to derive an optimal Q-former embedding q^* that satisfies a given **neural objective**, we perform iterative optimization in the pretrained Q-Former embedding space, guided by the differentiable encoding model Φ . This process evolves an initial image embedding toward one that elicits the desired brain response pattern. See Fig. 2.

We define neural objectives descriptively—for example, “maximize activation in FFA”, “co-activate FFA and PPA”, or “minimize response in the word-selective cortex”. Each

objective is realized by a task-specific loss function $\mathcal{L}_{\text{neuro}}$, computed on the predicted response $\Phi(q)$ for a given embedding q . For instance:

- **Maximize activation in region R :**

$$\mathcal{L}_{\text{neuro}}(\Phi(q)) = -\frac{1}{|R|} \sum_{v \in R} \Phi(q)_v$$

Given an initial embedding q^0 (e.g., derived from a random or reference image), we minimize this loss function via gradient descent:

$$q^{t+1} = q^t - \eta \nabla_q \mathcal{L}_{\text{neuro}}(\Phi(q^t)) \quad (2)$$

This yields a trajectory of embeddings $\{q^0, q^1, \dots, q^T\}$, each progressively aligning the predicted neural response with the target objective.

Because optimization is performed in the pretrained Q-Former space of a vision-language model, the search is naturally constrained by a semantically rich prior. This structure implicitly regularizes the process, guiding optimization toward realistic and interpretable solutions without requiring explicit regularization. Crucially, it allows direct optimization over embeddings to satisfy neural objectives. Without generating images or computing image-space gradients, making the process both efficient and flexible.

In the next section, we describe how this trajectory of optimized embeddings is used to condition a diffusion model yielding a visual pathway that captures how semantics evolve under neuro objectives.

3.3. Image Trajectory and Semantic Evolution

The optimization process yields a trajectory of embeddings in the Q-Former space, each progressively more aligned with the target neural objective. To visualize these embeddings as images, we leverage the pretrained, frozen BLIP-Diffusion model from [19], which supports Q-Former embedding-conditioned image generation. We keep the Null prompt “ ” for the diffusion process to ensure the generation is guided purely by our optimized embedding q , allowing us to observe how the representation evolves over time under neural constraints.

This produces a **semantic trajectory**—a coherent sequence of images illustrating how the visual stimulus evolves to better satisfy the target neural response. Early iterations typically yield subtle, interpretable edits relative to the starting image, while later stages converge toward maximally activating stimuli.

Importantly, this trajectory captures more than just the endpoint of optimization. It unifies *brain-guided image editing* and *preferred image synthesis* into a single process, revealing meaningful and structured intermediate representations along the path. This approach offers a novel lens into how structured visual features are shaped by programmable neural objectives.

4. Experiments

In this section, we validate NeuroVolve by replicating the known categorical or lower-order feature selectivity of visual regions along the hierarchy. Then we utilized NeuroVolve to analyze subject-specific features captured in the generated optimal images, highlighting the potential of creating personalized images that target a specific activation pattern for a specific individual. Finally we illustrated the capability of the model to generate images under curated neuro-objectives, including suppressing, co-activation of two regions and decoupling two regions.

4.1. Setup

We use the Natural Scenes Dataset (NSD)[1], which includes whole-brain 7T fMRI data from 8 subjects who viewed 10,000 naturalistic images from the MS COCO dataset. Of the 8 subjects, 4 subjects view the full 10,000 image set repeated 3 times. The brain activations were computed from the fMRI data using the GLMSingle algorithm [27]; each voxel’s response value is normalized per session ($\mu = 0, \sigma^2 = 1$). The brain activation to repeated images within a subject was averaged. The 9000 unique images for each subject are used to train the brain encoder Φ for each subject with the remaining 1000 shared images used to evaluate prediction accuracy via Pearson’s R . The image generation is on a per-subject basis; regional masks used in our experiments are the official NSD masks.

We utilize pretrained components from [20], including the frozen image encoder and Q-Former, along with the diffusion model from [19], which enables image generation conditioned on Q-Former embeddings. The model produces images at a resolution of 512×512 using 50 diffusion steps. To ensure that the generated images reflect only the semantics of the optimized embeddings, we use a Null prompt “ ” during both Q-Former embedding extraction and diffusion-based image generation. This setup ensures that the diffusion process is guided solely by the visual embedding, without textual influence. During embedding optimization, we run 300 gradient descent steps with a learning rate of 0.01.

4.2. Modulating activity in a single region

In this section, we first investigate how NeuroVolve can synthesize images under the simple objective of maximizing response in a single region. We test this across six visual regions of interest (ROIs): four higher-level areas—fusiform face area (FFA), extrastriate body area (EBA), mid-fusiform sulcus word area (mfswords), and parahippocampal place area (PPA)—as well as early visual areas V1 and V4. For each region, we start the optimization from the same set of random seed images. The results for four example seeds are shown in Fig. 3. The neural objective in this case is to maximize the average voxel response in the ROI, corresponding

to the following loss:

$$\mathcal{L}_{\text{neuro}}(\Phi(q)) = -\frac{1}{|R|} \sum_{v \in R} \Phi(q)_v$$

An example optimization trajectory is shown in Fig. 4, where we visualize images generated from embeddings sampled at *elbow points* along the optimization curve. Specifically, the images in Fig. 3 correspond to embeddings at 20%, 50%, 80%, and 100% progress toward the final neural objective. These snapshots illustrate how the visual representation evolves as the embedding increasingly aligns with the target brain response.

Qualitative inspection confirms that the semantic content of the synthesized images becomes increasingly aligned with the known preferences of the target regions. For example, FFA-optimized images progressively emphasize faces, while PPA converges on architectural or natural scene-like structures. These smooth, interpretable transitions demonstrate that NeuroVolve supports both preferred stimulus generation and image editing within a unified trajectory.

Importantly, NeuroVolve also captures fine-grained tuning in early visual areas, which are typically sensitive to low-level visual features. Optimized images for V1 prominently exhibit high-frequency textures, edge-like structures, and high-contrast patterns—consistent with its known functional role. Meanwhile V4-optimized images show richer color content, smooth gradients, and curvilinear shapes, aligning with its selectivity for color and complex form. These results demonstrate that NeuroVolve accurately reflects functional specialization across the visual hierarchy, from early visual areas to higher-order category-selective regions. Notably, this ability to recover low-level tuning through data-driven synthesis has not been demonstrated by prior brain-guided generative frameworks.

For the final optimized images, we evaluated both their predicted activation levels and semantic specificity. As shown in Fig. 5, the predicted responses in target regions consistently exceed those evoked by natural stimuli—demonstrating NeuroVolve’s ability to synthesize maximally activating content. In parallel, semantic classification results in Table 1 confirm that the generated images align with the expected functional preferences of each region.

4.3. Subject-Specific Maximizing Images

In Fig. 4 we observe that the optimization process reliably converges by the final iterations, suggesting the presence of stable optima in the embedding space under neural objectives. For certain ROIs, the resulting images are visually consistent across different seeds (Fig. 3), indicating strong semantic attractors shaped by the embedding space.

To evaluate subject-specificity, we synthesize optimal stimuli for the face-selective FFA and scene-selective PPA

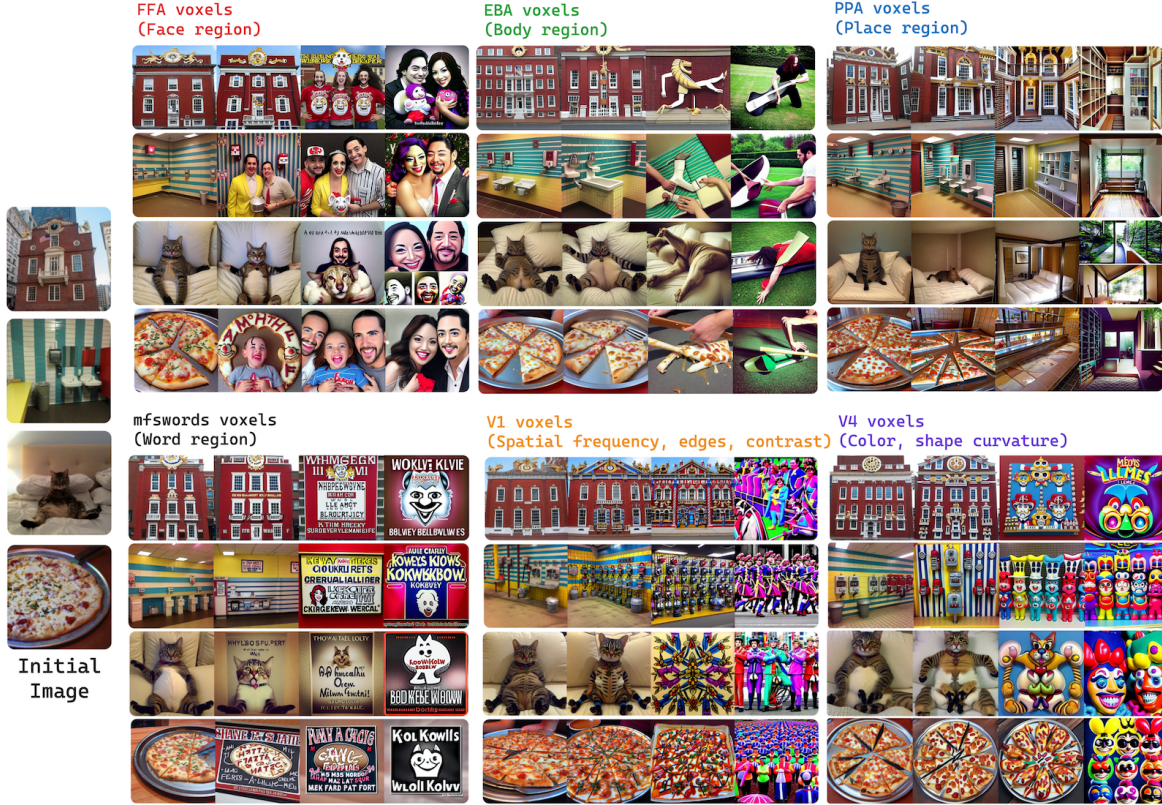


Figure 3. **Region-specific image evolution under neural objectives (S5).** Starting from the same seed images (left column), we optimize toward a neural objective of maximizing voxel activity in six distinct visual ROIs: FFA (faces), EBA (bodies), PPA (places), mfswords (words), V1 (edges, contrast), and V4 (color, curvature). NeuroVolve successfully evolves each input into semantically distinct outputs, reflecting the known selectivity of each region. Notably, our method captures both high-level semantic preferences (e.g., faces for FFA) and low-level visual features (e.g., high spatial frequency for V1, rich colors and curvature for V4). Demonstrating fine-grained, region-specific tuning across the visual hierarchy.

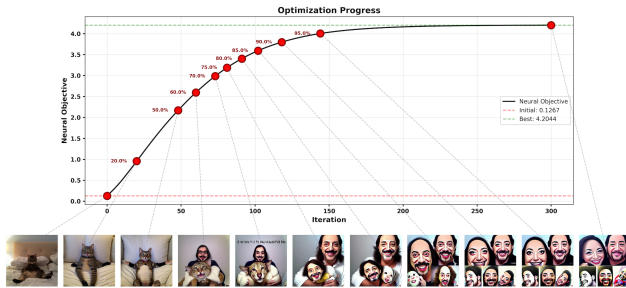


Figure 4. **NeuroVolve optimization trajectory for FFA.** The plot shows progress toward maximizing FFA activation. Images sampled along the trajectory reveal the semantic evolution from the initial input to a face-like stimulus. Illustrating how optimization reveals interpretable visual transitions under neural objective guidance.

across eight subjects. For each, we optimize from five random seed images and compare the final results to the top-5 predicted natural images (from 10,000 NSD stimuli), based

	Faces		Places		Bodies		Words	
	S2	S5	S2	S5	S2	S5	S2	S5
NSD all stim	17.1	17.5	29.4	30.7	31.5	30.3	11.0	10.1
NSD top-100	45.0	43.0	78.0	93.0	59.0	55.0	48.0	33.0
BrainDiVE-100	68.0	64.0	100	100	69.0	77.0	61.0	80.0
BrainSCUBA-100	67.0	62.0	100	99.0	54.0	73.0	55.0	34.0
NeuroVolve-100	100.0	99.0	100	100	54.0	92.0	95.0	34.0

Table 1. **Evaluating semantic specificity via zero-shot CLIP classification.** We use CLIP to classify images into four categories (faces, places, bodies, words) and report the percentage matching the target region’s preferred category. NSD rows report accuracy over all 10k natural images or the top-100 by true fMRI response. Model rows (BrainDiVE, BrainSCUBA, NeuroVolve) report accuracy over 100 generated images ranked by predicted activation. **NeuroVolve** outperforms the NSD top-1% and achieves the highest selectivity across most ROIs and subjects, demonstrating strong semantic selectivity.

on each subject’s encoding model.

As shown in Fig. 6, NeuroVolve consistently converges

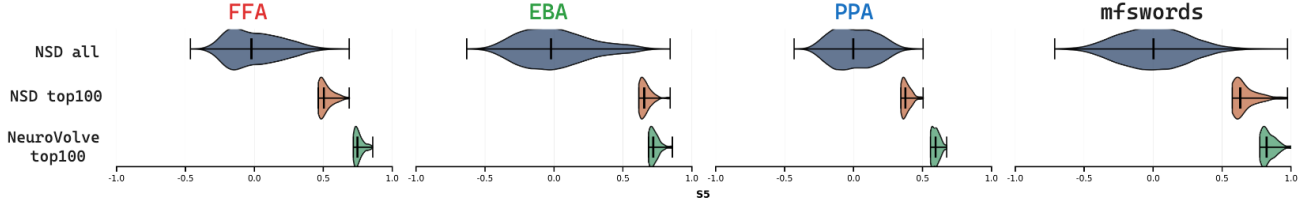


Figure 5. **Evaluating the distribution of NeuroVolve final images using an alternative encoder (ViT-H/14 CLIP).** We retrain the voxel-wise encoding model using a different vision backbone (ViT-H/14 CLIP) and evaluate predicted responses across image sets. For each region, we compare three distributions: (1) all NSD images seen by the subject, (2) the top-100 NSD images ranked by the ViT-H/14-based encoder, and (3) the top-100 NeuroVolve-generated images ranked by the same encoder. NeuroVolve images consistently achieve higher predicted activations. Pushing responses beyond those evoked by natural stimuli, demonstrating the model’s capacity to synthesize maximally activating content.

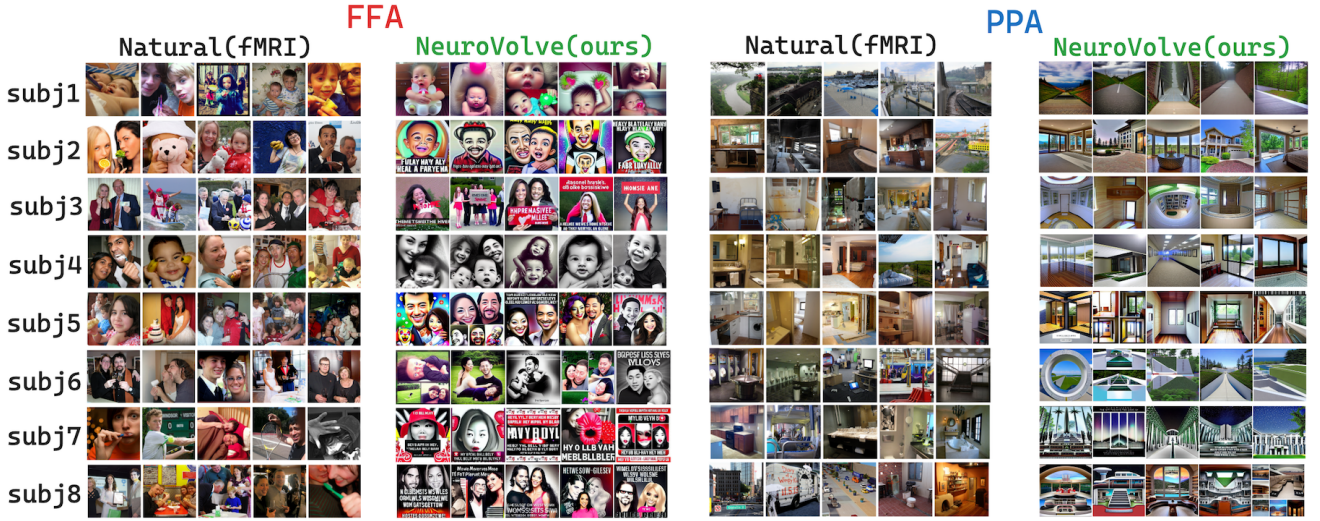


Figure 6. **Subject-specific optimization results for FFA and PPA (S1–S8).** For each region and subject, we show 5 optimized images (right), each initialized from a different random image, alongside the top-5 predicted natural images (left) based on the subject’s encoding model. NeuroVolve consistently converges to semantically similar solutions across seeds, aligning closely with top predicted natural stimuli and revealing subject-specific neural tuning.

to semantically coherent solutions across seeds, while also capturing distinct individual preferences. For example, Subject 1’s FFA favors baby faces, Subject 5 responds to group scenes, and Subjects 7–8 show FFA responses to text-like patterns—all mirrored in the synthesized outputs. Similarly, in PPA, some subjects prefer outdoor landscapes, while others respond more strongly to indoor environments.

Together, these results demonstrate that NeuroVolve not only generates interpretable, region-specific stimuli, but also models inter-subject variability in neural selectivity. This subject specificity emerges directly from embedding-space optimization using personalized encoding models, making NeuroVolve a powerful tool for individual brain-aligned synthesis.

4.4. Modulating activity with curated neural objectives

We next evaluated NeuroVolve’s ability to generate images that satisfy curated, programmable neural objectives beyond simple region-specific maximization. Specifically, we experimented with the following objectives: Suppressing the average voxel response in a single target region. Co-activating two distinct regions simultaneously. Activating one region while suppressing another. Each objective is implemented via a corresponding loss function $\mathcal{L}_{\text{neuro}}$, defined in terms of the predicted voxel responses from the neural encoder $\Phi(q)$:

- **Suppress activation in region R :**

$$\mathcal{L}_{\text{neuro}}(q) = \frac{1}{|R|} \sum_{v \in R} \Phi(q)_v$$



Figure 7. **Image synthesis under curated neural objectives.** We show NeuroVolve generated images for various brain-guided objectives: suppressing a single region (−ROI), co-activating two regions (+ROI1+ROI2), or activating one region while suppressing another (+ROI1−ROI2 or −ROI1+ROI2). Red labels indicate suppression, green labels indicate activation. These results highlight NeuroVolve’s flexibility in generating semantically coherent images that satisfy complex neural constraints.

- **Co-activate R_1 and R_2 :**

$$\mathcal{L}_{\text{neuro}}(q) = - \left(\lambda_1 \cdot \frac{1}{|R_1|} \sum_{v \in R_1} \Phi(q)_v + \lambda_2 \cdot \frac{1}{|R_2|} \sum_{v \in R_2} \Phi(q)_v \right)$$

- **Activate R_1 while suppressing R_2 :**

$$\mathcal{L}_{\text{neuro}}(q) = -\lambda_1 \cdot \frac{1}{|R_1|} \sum_{v \in R_1} \Phi(q)_v + \lambda_2 \cdot \frac{1}{|R_2|} \sum_{v \in R_2} \Phi(q)_v$$

These curated objectives allow us to probe fine-grained patterns of cooperative and antagonistic tuning across visual regions, demonstrating how NeuroVolve can flexibly steer image synthesis under compositional, brain-derived constraints. In Fig. 7, we show generated results for a single seed image under nine distinct neural objectives.

A visual inspection reveals systematic changes aligned with the intended objectives. In co-activation settings, the resulting images incorporate features corresponding to both regions—capturing a mixture of semantic and low-level visual selectivity. In contrast, when one region is activated while another is suppressed, we observe one feature set diminishing as the other becomes more prominent.

These results demonstrate that NeuroVolve can generate synthetic images predicted to jointly satisfy complex, multi-region neural objectives—often achieving levels of predicted activation not attainable with natural stimuli. This highlights the method’s potential as a tool for data-driven exploration of more complex and fine-grained neural response patterns in the human visual cortex.

5. Conclusions

We introduce NeuroVolve, a flexible framework for synthesizing images under programmable neural objectives. NeuroVolve enables the specification of complex neural targets—including activation, suppression, and co-activation across single or multiple brain regions—allowing fine-grained, data-driven probing of cortical representations beyond traditional single-region maximization.

By optimizing in the semantically rich embedding space of a vision-language model and conditioning a diffusion generator, NeuroVolve efficiently produces images that reflect complex neural targets. This enables more precise characterization of both low-level and semantic tuning preferences across the visual system. Importantly, the optimization process yields a *semantic trajectory* of intermediate embeddings, revealing interpretable visual transitions and unifying brain-guided image editing with preferred stimulus generation.

We demonstrate that NeuroVolve can recover known selectivity in high-level areas, uniquely capture tuning in early visual regions, and generate coherent stimuli under curated multi-region constraints. Furthermore, we showed that the framework captures subject-specific neural preferences, revealing individual variability in visual tuning.

These capabilities establish NeuroVolve as a powerful tool for data-driven cortical mapping, personalized brain-aligned generation, and broader applications in neuroscience, diagnostics, and brain-computer interfaces.

References

- [1] Emily J Allen, Ghislain St-Yves, Yihan Wu, Jesse L Breedlove, Jacob S Prince, Logan T Dowdle, Matthias Nau, Brad Caron, Franco Pestilli, Ian Charest, et al. A massive

- 7t fmri dataset to bridge cognitive neuroscience and artificial intelligence. *Nature neuroscience*, 25(1):116–126, 2022. 5
- [2] Pouya Bashivan, Kohitij Kar, and James J DiCarlo. Neural population control via deep image synthesis. *Science*, 364(6439):eaav9436, 2019. 3
- [3] Diego García Cerdas, Christina Sartzetaki, Magnus Petersen, Gemma Roig, Pascal Mettes, and Iris Groen. Brainactiv: Identifying visuo-semantic properties driving cortical selectivity using diffusion-based image manipulation. *bioRxiv*, pages 2024–10, 2024. 2, 3
- [4] Colin Conwell, Jacob S Prince, Kendrick N Kay, George A Alvarez, and Talia Konkle. What can 1.8 billion regressions tell us about the pressures shaping high-level visual representation in brains and machines? *BioRxiv*, pages 2022–03, 2022. 2, 4
- [5] Gregory C DeAngelis, Izumi Ohzawa, and Ralph D Freeman. Receptive-field dynamics in the central visual pathways. *Trends in neurosciences*, 18(10):451–458, 1995. 2
- [6] Michael Eickenberg, Alexandre Gramfort, Gaël Varoquaux, and Bertrand Thirion. Seeing it all: Convolutional network layers map the function of the human visual system. *NeuroImage*, 152:184–194, 2017. 2
- [7] Russell Epstein and Nancy Kanwisher. A cortical representation of the local visual environment. *Nature*, 392(6676):598–601, 1998. 2
- [8] Ian Goodfellow, Jean Pouget-Abadie, Mehdi Mirza, Bing Xu, David Warde-Farley, Sherjil Ozair, Aaron Courville, and Yoshua Bengio. Generative adversarial networks. *Communications of the ACM*, 63(11):139–144, 2020. 2
- [9] Kalanit Grill-Spector and Rafael Malach. The human visual cortex. *Annual Review of Neuroscience*, 27:649–677, 2004. 2
- [10] Kalanit Grill-Spector and Rafael Malach. The human visual cortex. *Annu. Rev. Neurosci.*, 27(1):649–677, 2004. 2
- [11] Zijin Gu, Keith Wakefield Jamison, Meenakshi Khosla, Emily J Allen, Yihan Wu, Ghislain St-Yves, Thomas Naselaris, Kendrick Kay, Mert R Sabuncu, and Amy Kuceyeski. Neurogen: activation optimized image synthesis for discovery neuroscience. *NeuroImage*, 247:118812, 2022. 2, 3
- [12] Jonathan Ho, Chitwan Saharia, William Chan, David J Fleet, Mohammad Norouzi, and Tim Salimans. Cascaded diffusion models for high fidelity image generation. *J. Mach. Learn. Res.*, 23(47):1–33, 2022. 2
- [13] David H Hubel and Torsten N Wiesel. Receptive fields of single neurones in the cat’s striate cortex. *The Journal of physiology*, 148(3):574, 1959. 2
- [14] Alexander G Huth, Shinji Nishimoto, An T Vu, and Jack L Gallant. A continuous semantic space describes the representation of thousands of object and action categories across the human brain. *Neuron*, 76(6):1210–1224, 2012. 2
- [15] A Ishai, L G Ungerleider, A Martin, J L Schouten, and J V Haxby. Distributed representation of objects in the human ventral visual pathway. *Proc Natl Acad Sci U S A*, 96(16):9379–9384, 1999. 2
- [16] Nidhi Jain, Aria Wang, Margaret M Henderson, Ruogu Lin, Jacob S Prince, Michael J Tarr, and Leila Wehbe. Selectivity for food in human ventral visual cortex. *Communications Biology*, 6(1):175, 2023. 2
- [17] Nancy Kanwisher, Josh McDermott, and Marvin M Chun. The fusiform face area: a module in human extrastriate cortex specialized for face perception. *Journal of neuroscience*, 17(11):4302–4311, 1997.
- [18] Meenakshi Khosla, N Apurva Ratan Murty, and Nancy Kanwisher. A highly selective response to food in human visual cortex revealed by hypothesis-free voxel decomposition. *Current Biology*, 32(19):4159–4171, 2022. 2
- [19] Dongxu Li, Junnan Li, and Steven Hoi. Blip-diffusion: Pre-trained subject representation for controllable text-to-image generation and editing. *Advances in Neural Information Processing Systems*, 36:30146–30166, 2023. 3, 4, 5
- [20] Junnan Li, Dongxu Li, Silvio Savarese, and Steven Hoi. Blip-2: Bootstrapping language-image pre-training with frozen image encoders and large language models. In *International conference on machine learning*, pages 19730–19742. PMLR, 2023. 2, 3, 4, 5
- [21] Andrew Luo, Maggie Henderson, Leila Wehbe, and Michael Tarr. Brain diffusion for visual exploration: Cortical discovery using large scale generative models. *Advances in Neural Information Processing Systems*, 36:75740–75781, 2023. 2, 3
- [22] Andrew F Luo, Margaret M Henderson, Michael J Tarr, and Leila Wehbe. Brainscuba: Fine-grained natural language captions of visual cortex selectivity. *arXiv preprint arXiv:2310.04420*, 2023. 2, 3
- [23] J Anthony Movshon, ID Thompson, and DJ Tolhurst. Spatial and temporal contrast sensitivity of neurones in areas 17 and 18 of the cat’s visual cortex. *The Journal of physiology*, 283(1):101–120, 1978. 2
- [24] Thomas Naselaris, Kendrick N Kay, Shinji Nishimoto, and Jack L Gallant. Encoding and decoding in fmri. *Neuroimage*, 56(2):400–410, 2011. 2
- [25] Ian ML Pennock, Chris Racey, Emily J Allen, Yihan Wu, Thomas Naselaris, Kendrick N Kay, Anna Franklin, and Jenny M Bosten. Color-biased regions in the ventral visual pathway are food selective. *Current Biology*, 33(1):134–146, 2023. 2
- [26] Carlos R Ponce, Will Xiao, Peter F Schade, Till S Hartmann, Gabriel Kreiman, and Margaret S Livingstone. Evolving images for visual neurons using a deep generative network reveals coding principles and neuronal preferences. *Cell*, 177(4):999–1009, 2019. 3
- [27] Jacob S Prince, Ian Charest, Jan W Kurzwaski, John A Pyles, Michael J Tarr, and Kendrick N Kay. Improving the accuracy of single-trial fmri response estimates using glmsingle. *Elife*, 11:e77599, 2022. 5
- [28] N Apurva Ratan Murty, Pouya Bashivan, Alex Abate, James J DiCarlo, and Nancy Kanwisher. Computational models of category-selective brain regions enable high-throughput tests of selectivity. *Nature communications*, 12(1):5540, 2021. 2, 3
- [29] Justine Sergeant, Shinsuke Ohta, and Brennan Macdonald. Functional neuroanatomy of face and object processing: a positron emission tomography study. *Brain*, 115(1):15–36, 1992. 2
- [30] Yang Song, Jascha Sohl-Dickstein, Diederik P Kingma, Abhishek Kumar, Stefano Ermon, and Ben Poole. Score-based

generative modeling through stochastic differential equations. *arXiv preprint arXiv:2011.13456*, 2020. [2](#)

- [31] Edgar Y Walker, Fabian H Sinz, Erick Cobos, Taliah Muhammad, Emmanouil Froudarakis, Paul G Fahey, Alexander S Ecker, Jacob Reimer, Xaq Pitkow, and Andreas S Tolias. Inception loops discover what excites neurons most using deep predictive models. *Nature neuroscience*, 22(12):2060–2065, 2019. [3](#)
- [32] Aria Y Wang, Kendrick Kay, Thomas Naselaris, Michael J Tarr, and Leila Wehbe. Better models of human high-level visual cortex emerge from natural language supervision with a large and diverse dataset. *Nature Machine Intelligence*, 5(12):1415–1426, 2023. [2](#), [4](#)
- [33] Daniel LK Yamins, Ha Hong, Charles F Cadieu, Ethan A Solomon, Darren Seibert, and James J DiCarlo. Performance-optimized hierarchical models predict neural responses in higher visual cortex. *Proceedings of the national academy of sciences*, 111(23):8619–8624, 2014. [2](#)

A. Supplemental

Sections

1. Additional Results: Fine-Grained Face-Region Selectivity (FFA vs. OFA) ([A.1](#))
2. Ablation: Random Initialization in Q-Former Embedding Space ([A.2](#))
3. Neural Encoding Model training and validation ([A.3](#))
4. Visualization of each subject’s selective voxel images ([A.4](#))
5. Semantic classification setup and results ([A.5](#))
6. Activation Comparison of Final Generated Images ([A.6](#))
7. Optimization Trajectories ([A.7](#))

A.1. Additional Results: Fine-Grained Face-Region Selectivity (FFA vs. OFA)

In this section, we visualize generated images obtained by maximizing voxel responses in the FFA and OFA. All images are produced from randomly initialized embeddings in the BLIP Q-former space. We observe that the optimization process captures fine-grained differences between these two face-selective regions: FFA-optimized images tend to depict more realistic human faces, whereas OFA-optimized images more often resemble animated, or mask-like faces or animals faces. Subject-specific comparisons are shown below. These results demonstrate that our method can reliably highlight subtle differences in semantic selectivity across closely related regions.

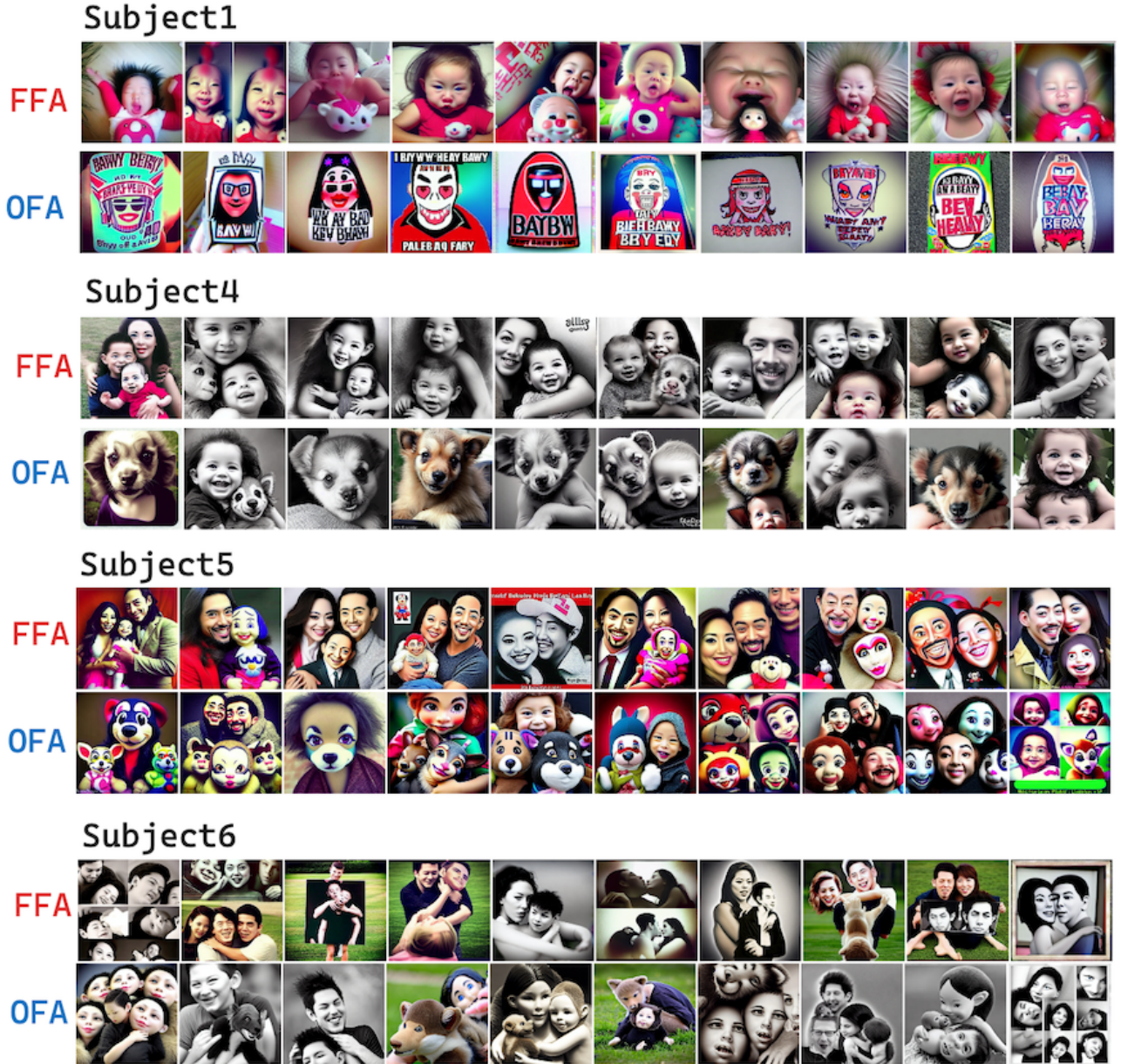


Figure S1. **Comparison between images generated by activating FFA versus OFA.** Our method captures fine-grained differences across face-selective regions: optimization toward maximizing FFA responses produces more realistic human faces, whereas optimization toward maximizing OFA responses yields more abstract, stylized, or animal-like faces.

A.2. Ablation: Random Initialization in Q-Former Embedding Space

Here we present an ablation study in which, instead of initializing the optimization from the embedding of a seed image, we begin from a randomly initialized embedding in the Q-Former space. This setup isolates the contribution of the optimization itself, independent of any semantic structure inherited from a seed-image starting point. The neuro-objective is to maximize the predicted response within each target region.

Across subjects and ROIs, we find that NeuroVolve reliably converges to solutions that capture the characteristic selectivity of the targeted voxels, regardless of initialization. These results demonstrate the robustness of our method and its ability to identify functionally meaningful embeddings in Q-Former space even when starting from an uninformed random point.

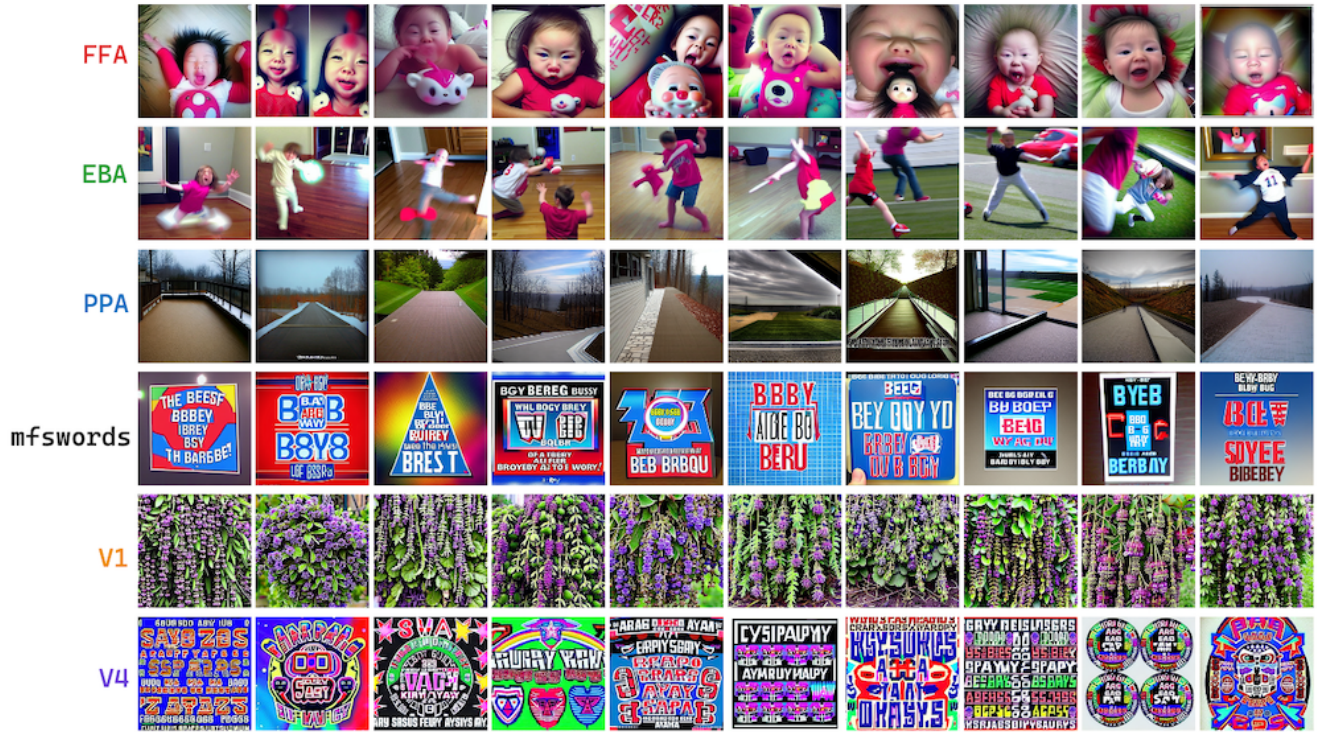


Figure S2. Random start NeuroVolve S1.



Figure S3. Random start NeuroVolve S2.

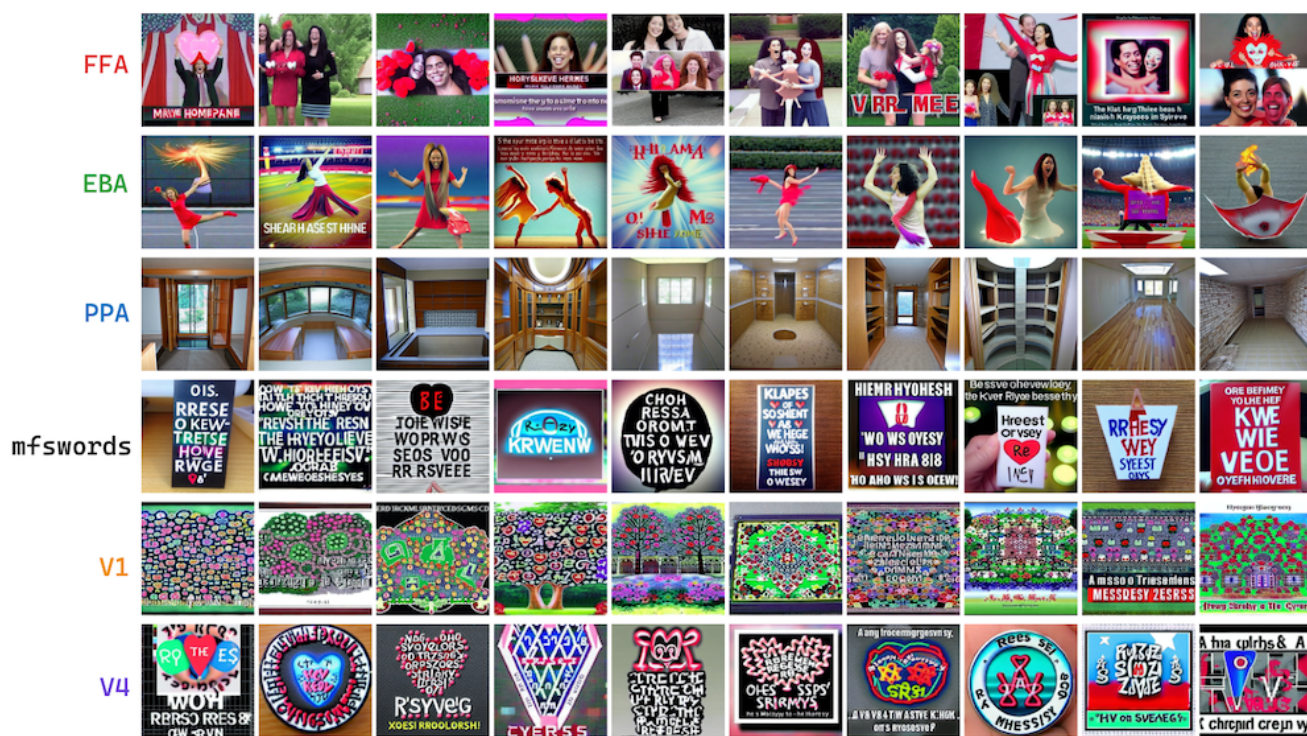


Figure S4. Random start NeuroVolve S3.

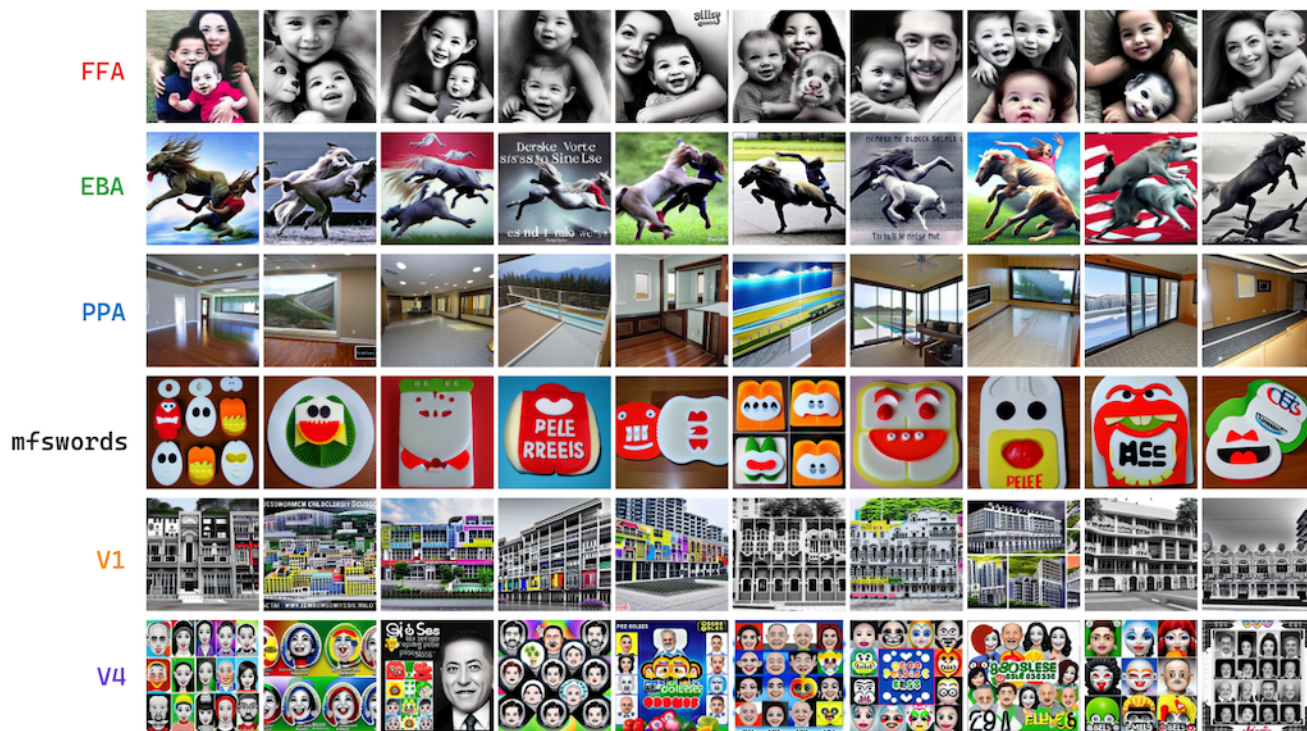


Figure S5. Random start NeuroVolve S4.

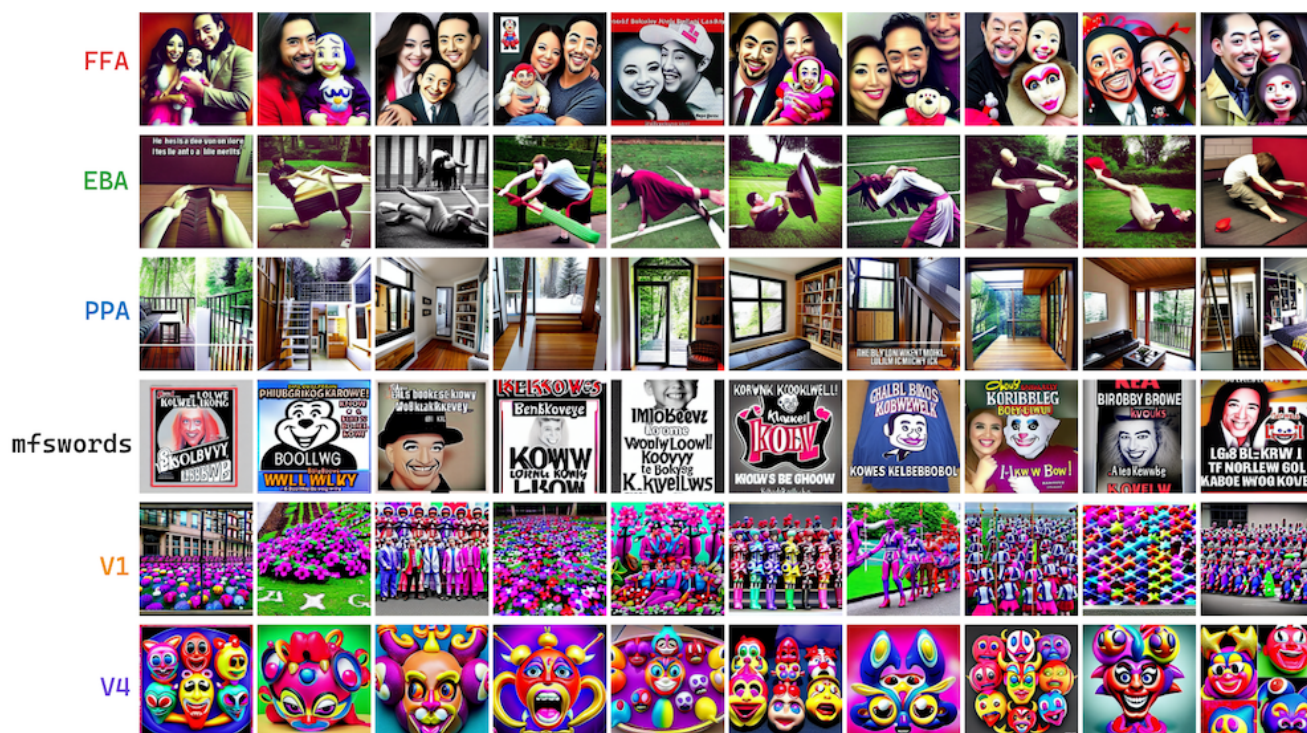


Figure S6. Random start NeuroVolve S5.

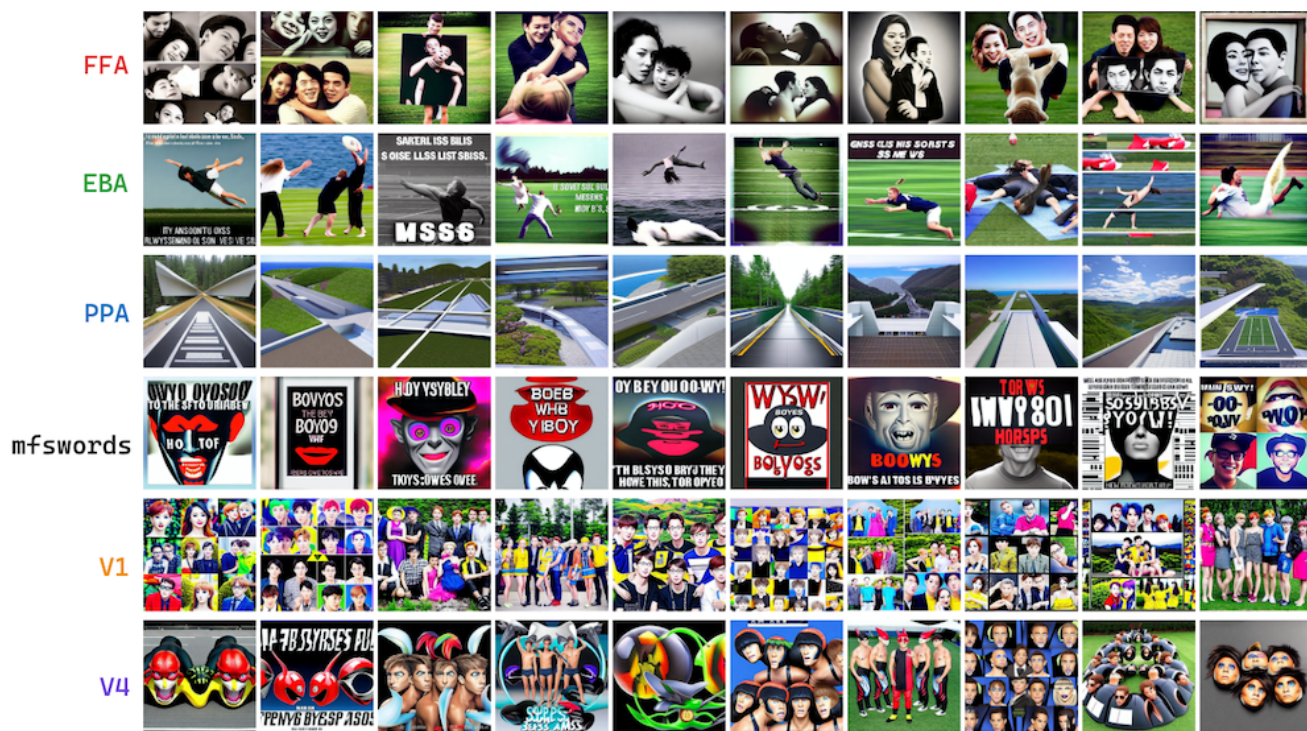


Figure S7. Random start NeuroVolve S6.



Figure S8. Random start NeuroVolve S7.

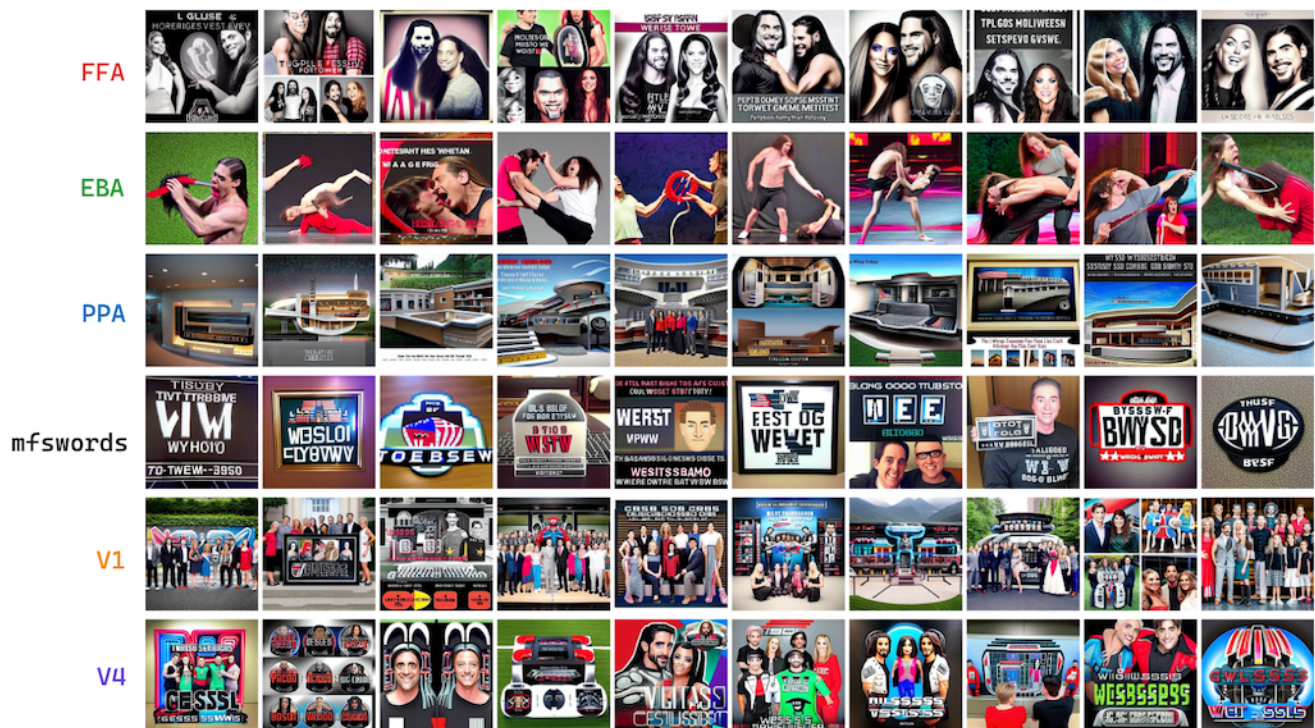


Figure S9. Random start NeuroVolve S8.

A.3. Neural Encoding model training and validation

Neural Encoding Model Implementation Our neural encoding model consists of two main components:

1. **Frozen Backbone.** We use the pretrained BLIP-2 encoder, comprising an image encoder and the Q-Former (query transformer), as a frozen backbone to extract image embeddings.
2. **Voxelwise Prediction Module Φ (MLP).**
 - **Input Projection.** The image embedding extracted from the Q-Former has a shape of 16×768 . We flatten it into a 1D vector and pass it through a three-layer MLP with hidden dimensions of 2048, 1024, and 512. ReLU activations are applied between layers, outputting a 512-dimensional embedding.
 - **Readout Layer.** The 512-dimensional embedding is passed through a linear readout layer that maps it to \mathbb{R}^N , where N denotes the number of voxels being predicted. In our setup, this includes all voxels within the visual cortex, spanning both early visual areas and higher-order visual regions.

Model Training We train the encoding model using the AdamW optimizer with a learning rate of 3×10^{-4} . Training proceeds for up to 50 epochs, with early stopping applied if the validation accuracy fails to improve for 5 consecutive epochs. Each subject’s model is trained independently using approximately 9,000 subject-specific image–fMRI response pairs from their unique stimulus set. Model performance is evaluated on a shared validation set of roughly 1,000 images common to all subjects. We use a batch size of 32 image embeddings per training step.

Encoder Voxelwise Prediction Accuracy We report the voxelwise pearson correlation (R) as the encoding accuracy. The neural encoding models evaluated on the held-out test images. Our model predicts responses for voxels across both early visual cortex and higher-order visual regions, achieving high correlation scores throughout the visual cortex.

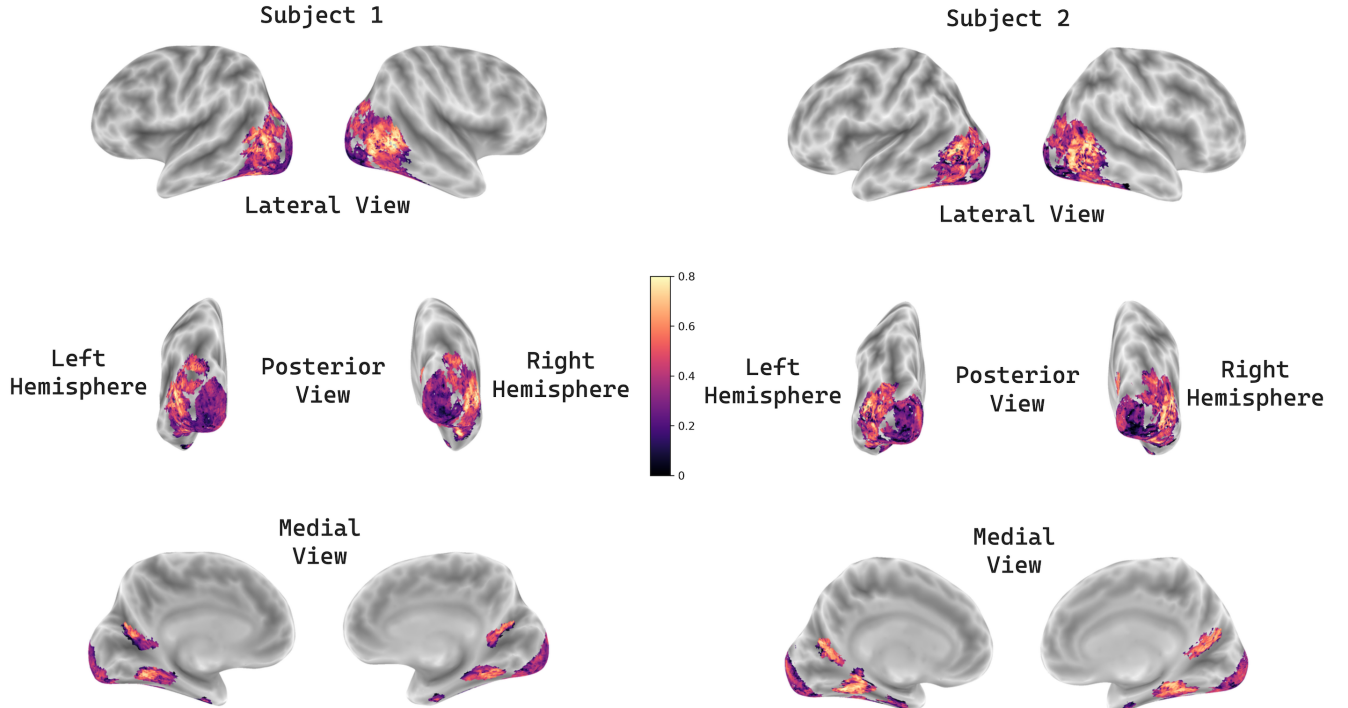


Figure S10. **Neural encoding model accuracy for S1–S2.** Voxelwise prediction accuracy is evaluated using pearson correlation (R) on $\sim 1,000$ shared test images. The model includes voxels across early visual and higher-order visual areas. Voxels outside the visual cortex are not modeled.

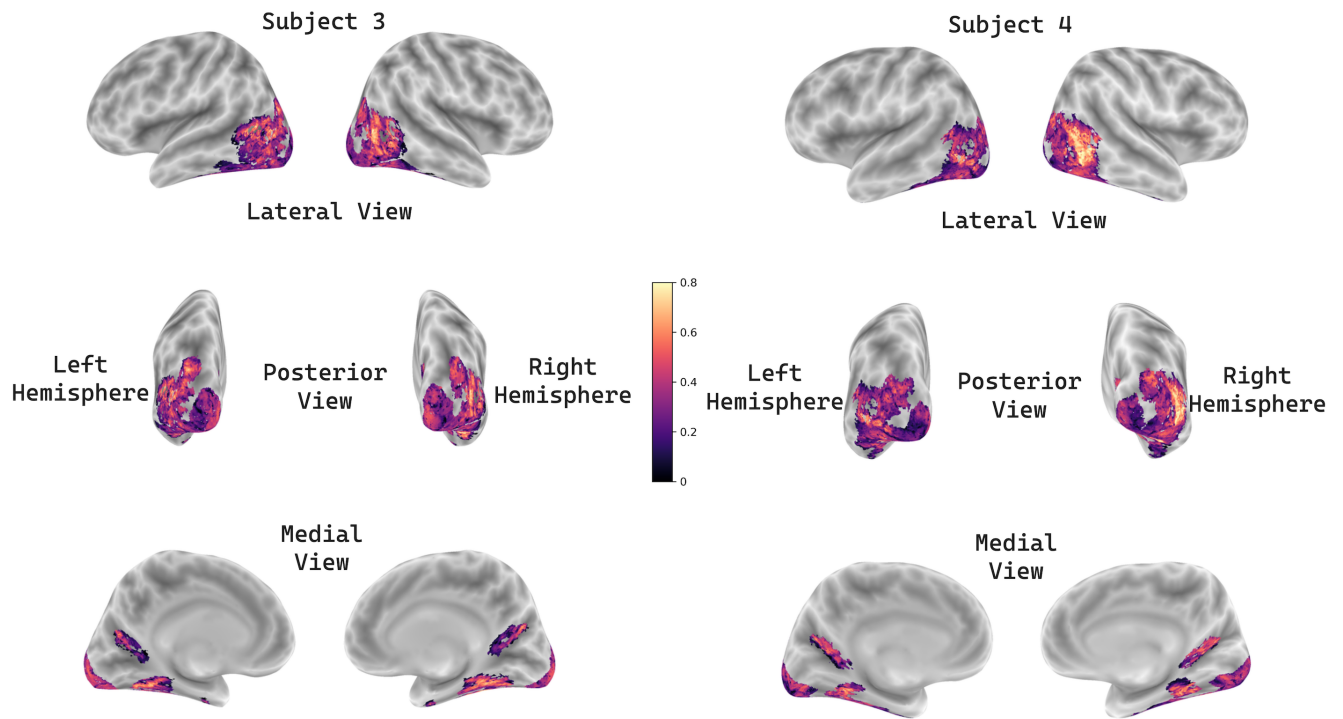


Figure S11. **Neural encoding model accuracy for S3-S4.** Voxelwise prediction accuracy is evaluated using Pearson correlation (R) on $\sim 1,000$ shared test images. The model includes voxels across early visual and higher-order visual areas. Voxels outside the visual cortex are not modeled.

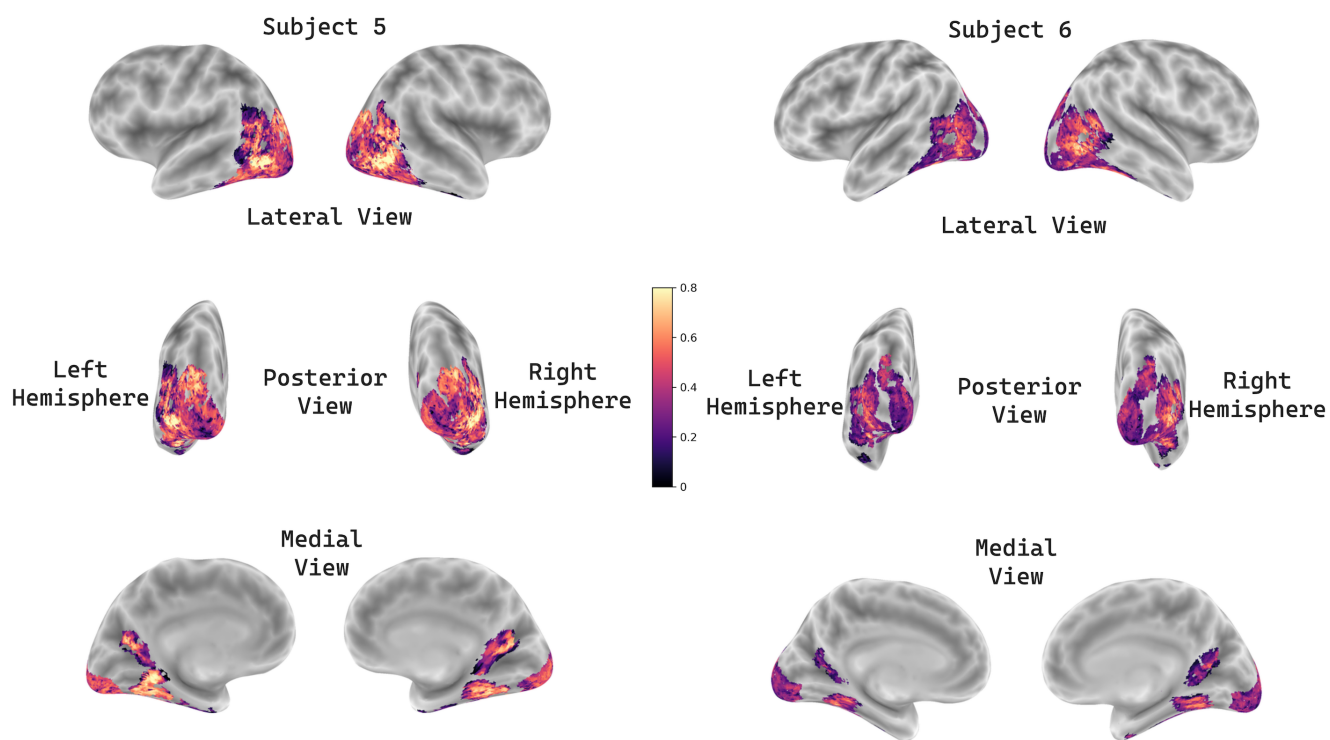


Figure S12. **Neural encoding model accuracy for S5-S6.** Voxelwise prediction accuracy is evaluated using Pearson correlation (R) on $\sim 1,000$ shared test images. The model includes voxels across early visual and higher-order visual areas. Voxels outside the visual cortex are not modeled.

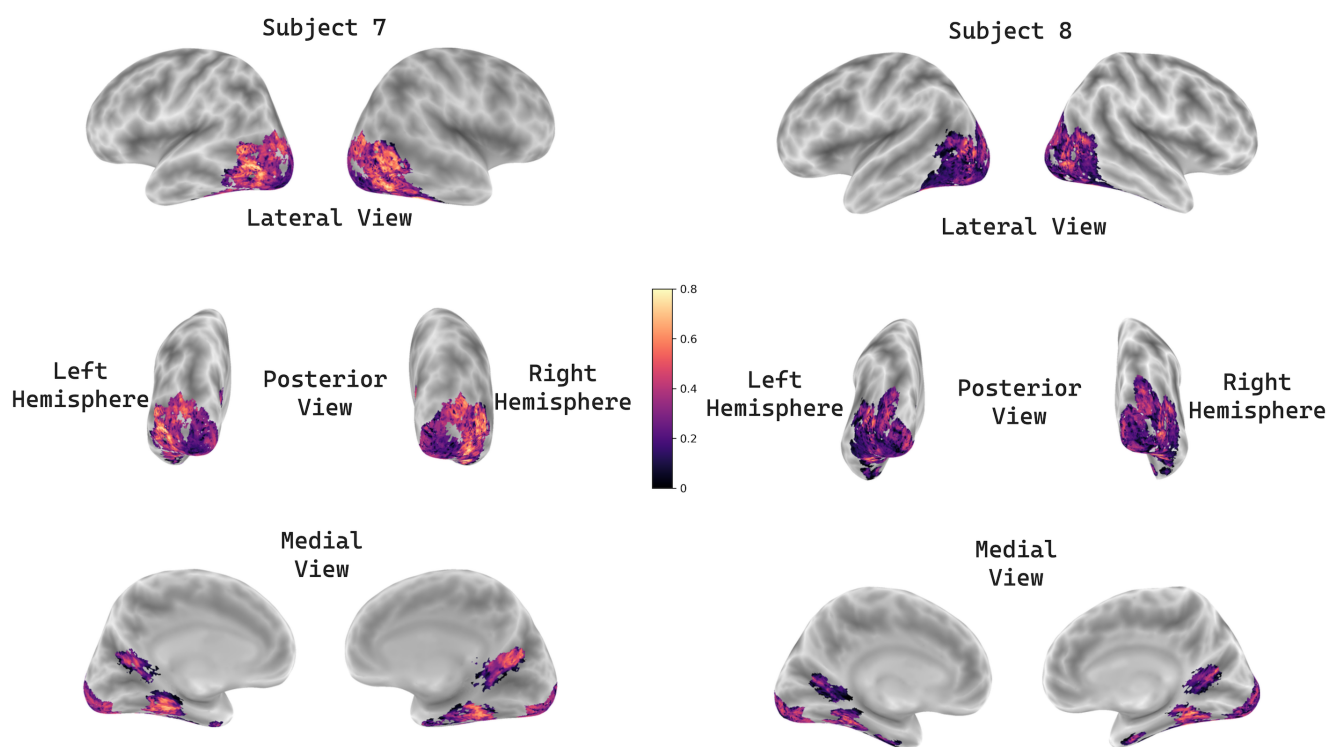


Figure S13. **Neural encoding model accuracy for S7-S8.** Voxelwise prediction accuracy is evaluated using Pearson correlation (R) on $\sim 1,000$ shared test images. The model includes voxels across early visual and higher-order visual areas. Voxels outside the visual cortex are not modeled.

A.4. Visualization of each subject's selective voxel images

We visualize the generated images for each subject under the neural objective of maximizing the predicted voxel response within the selected ROIs. For each region, the optimization reliably produces images that capture the characteristic selectivity of the targeted voxel set, demonstrating the model's ability to synthesize region-specific, functionally meaningful stimuli across subjects. For each optimization trajectory, we show images corresponding to the embedding at 20%, 50%, 80%, and 100% progress toward the final neural objective. These snapshots illustrate how the visual representation evolves as the embedding becomes increasingly aligned with the target brain response.

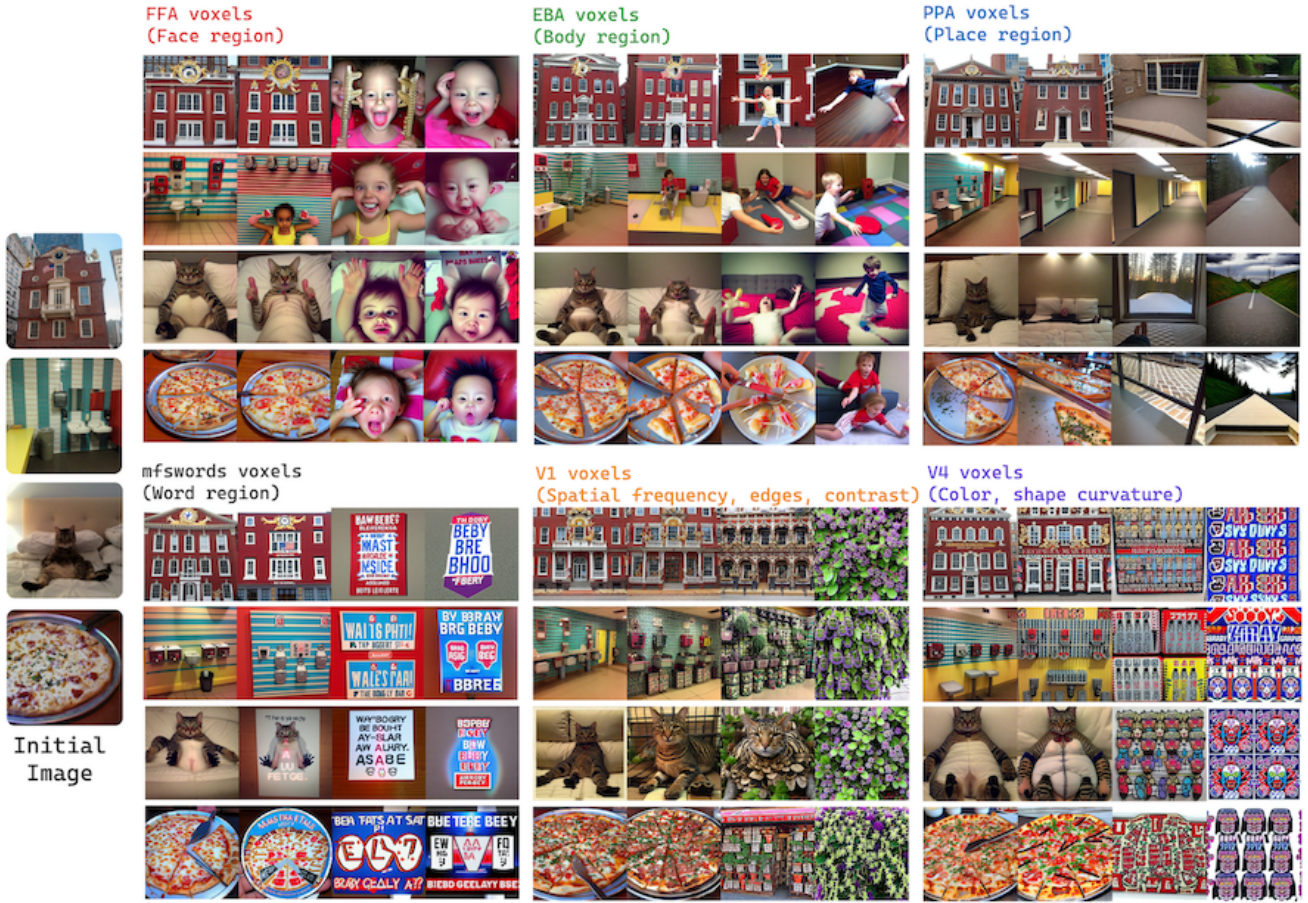


Figure S14. **Region-specific image evolution under neural objectives (S1).** Starting from the same seed images (left column), we optimize toward a neural objective of maximizing voxel activity in six distinct visual ROIs: FFA (faces), EBA (bodies), PPA (places), mfswords (words), V1 (edges/contrast), and V4 (color/curvature). For each ROI, we show the generated images at **20%, 50%, 80%, and 100%** progress along the optimization trajectory, illustrating how the visual representation gradually evolves as the embedding aligns with the target neural response.

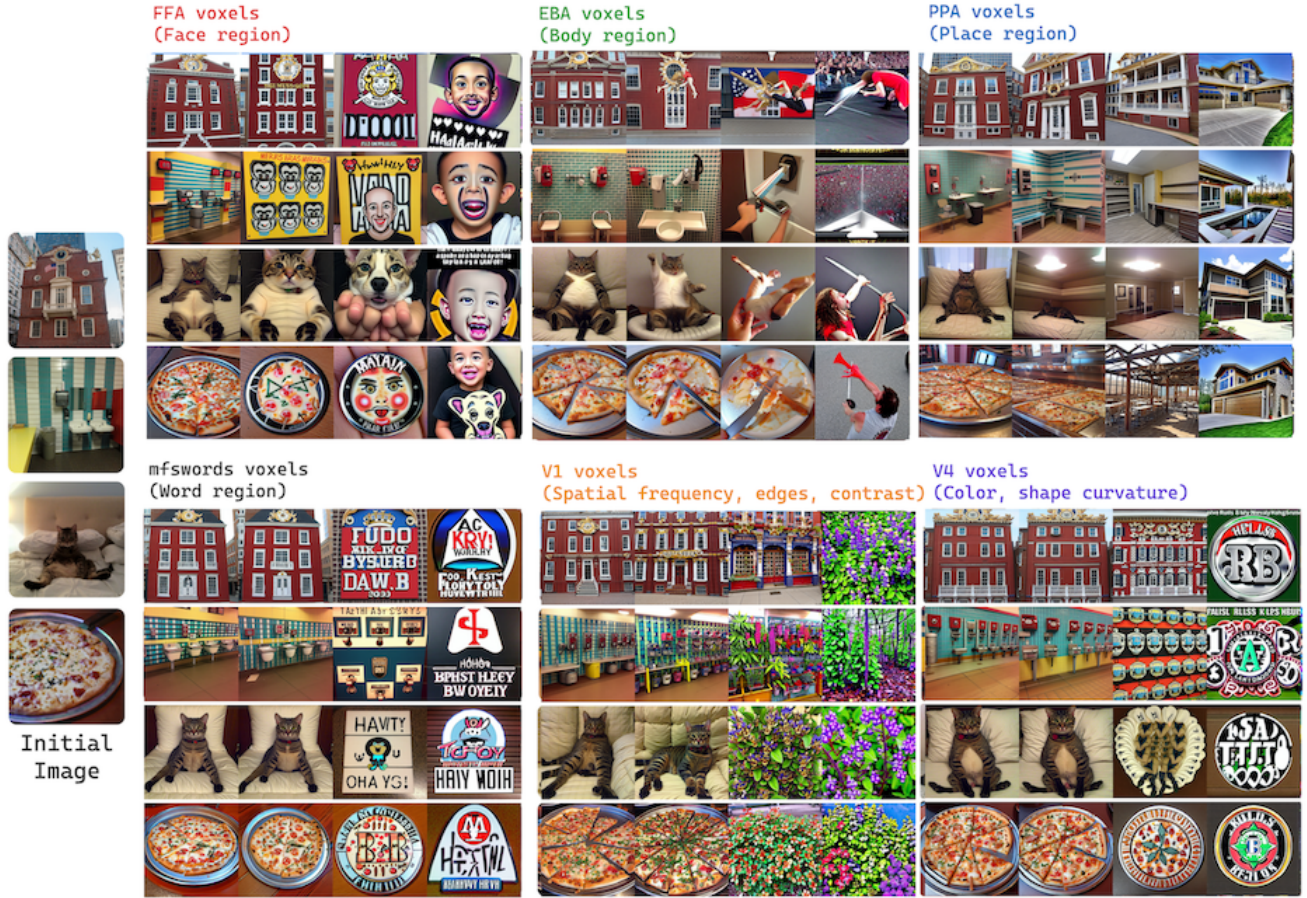


Figure S15. **Region-specific image evolution under neural objectives (S2).** Starting from the same seed images (left column), we optimize toward a neural objective of maximizing voxel activity in six distinct visual ROIs: FFA (faces), EBA (bodies), PPA (places), mfswords (words), V1 (edges/contrast), and V4 (color/curvature). For each ROI, we show the generated images at **20%, 50%, 80%, and 100%** progress along the optimization trajectory, illustrating how the visual representation gradually evolves as the embedding aligns with the target neural response.

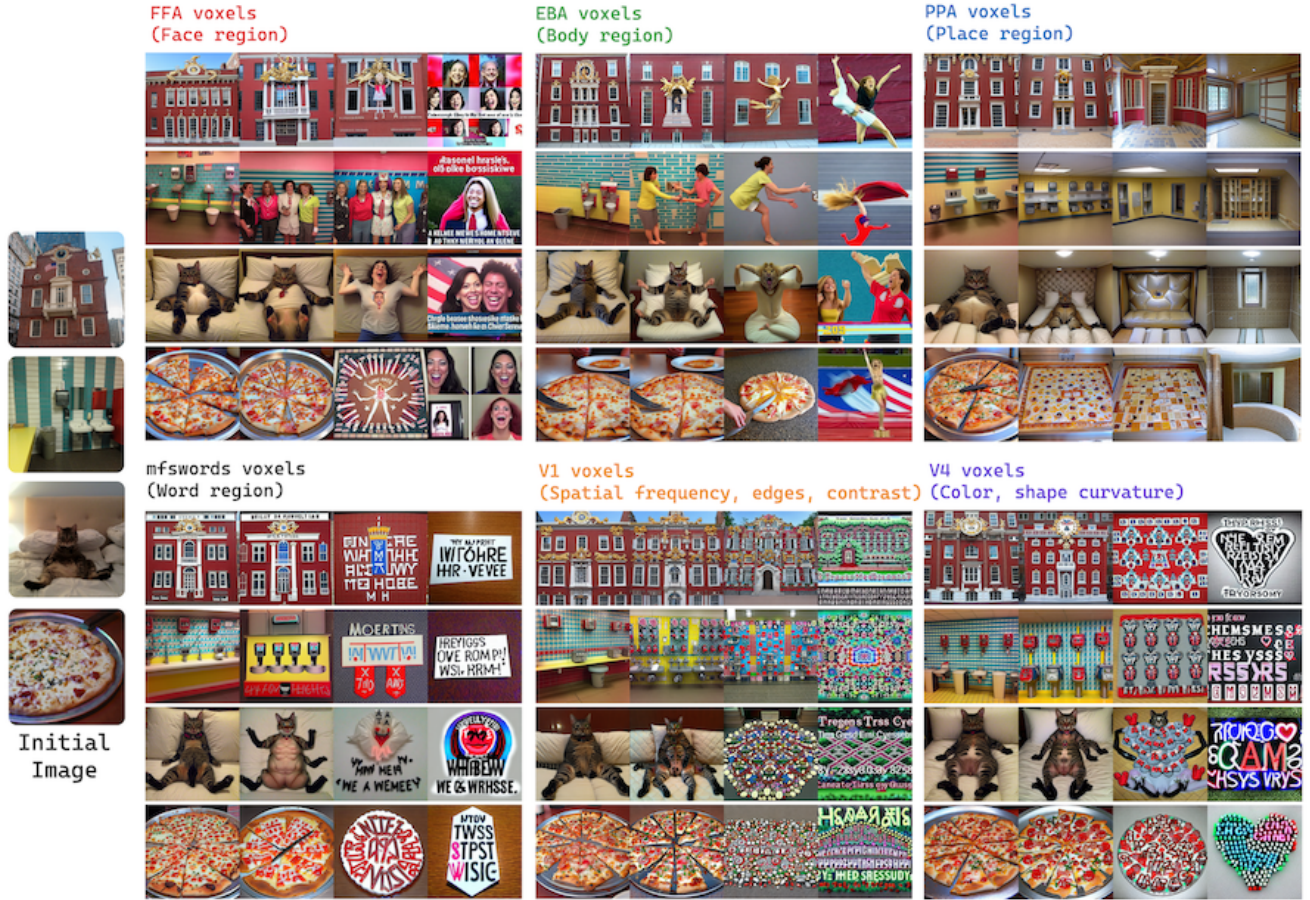


Figure S16. **Region-specific image evolution under neural objectives (S3).** Starting from the same seed images (left column), we optimize toward a neural objective of maximizing voxel activity in six distinct visual ROIs: FFA (faces), EBA (bodies), PPA (places), mfswords (words), V1 (edges/contrast), and V4 (color/curvature). For each ROI, we show the generated images at **20%, 50%, 80%, and 100%** progress along the optimization trajectory, illustrating how the visual representation gradually evolves as the embedding aligns with the target neural response.

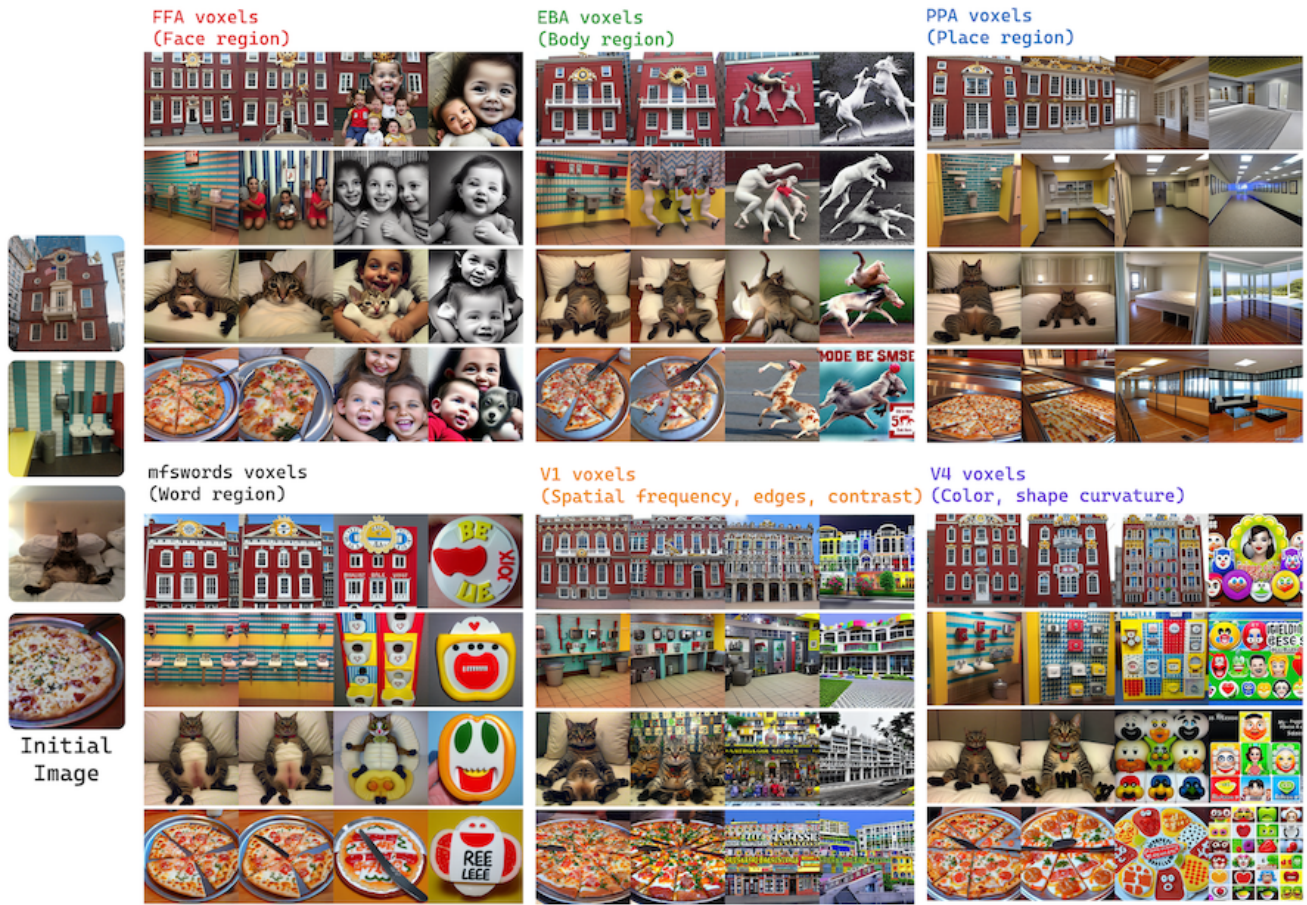


Figure S17. **Region-specific image evolution under neural objectives (S4).** Starting from the same seed images (left column), we optimize toward a neural objective of maximizing voxel activity in six distinct visual ROIs: FFA (faces), EBA (bodies), PPA (places), mfswords (words), V1 (edges/contrast), and V4 (color/curvature). For each ROI, we show the generated images at **20%, 50%, 80%, and 100%** progress along the optimization trajectory, illustrating how the visual representation gradually evolves as the embedding aligns with the target neural response.

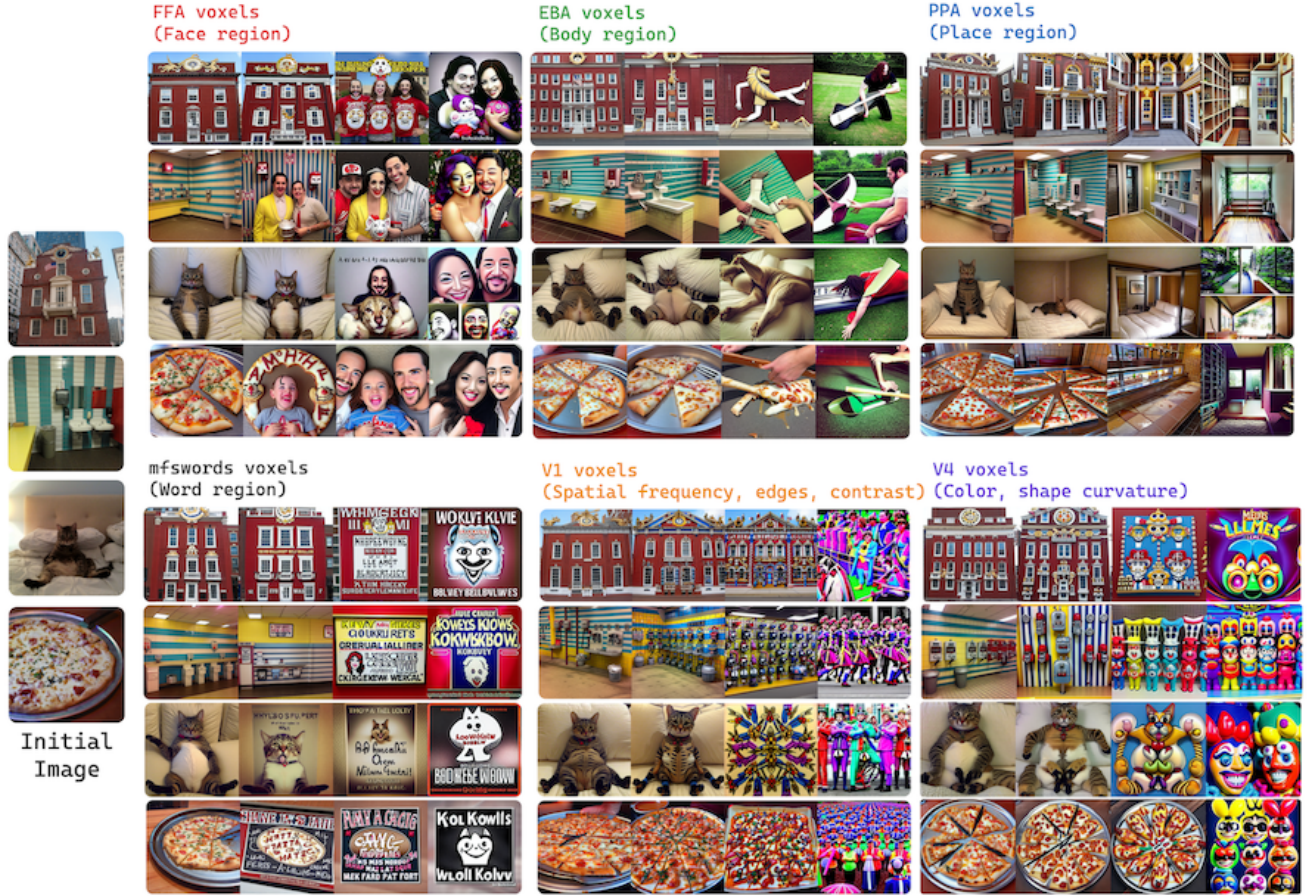


Figure S18. **Region-specific image evolution under neural objectives (S5).** Starting from the same seed images (left column), we optimize toward a neural objective of maximizing voxel activity in six distinct visual ROIs: FFA (faces), EBA (bodies), PPA (places), mfswords (words), V1 (edges/contrast), and V4 (color/curvature). For each ROI, we show the generated images at **20%, 50%, 80%, and 100%** progress along the optimization trajectory, illustrating how the visual representation gradually evolves as the embedding aligns with the target neural response.

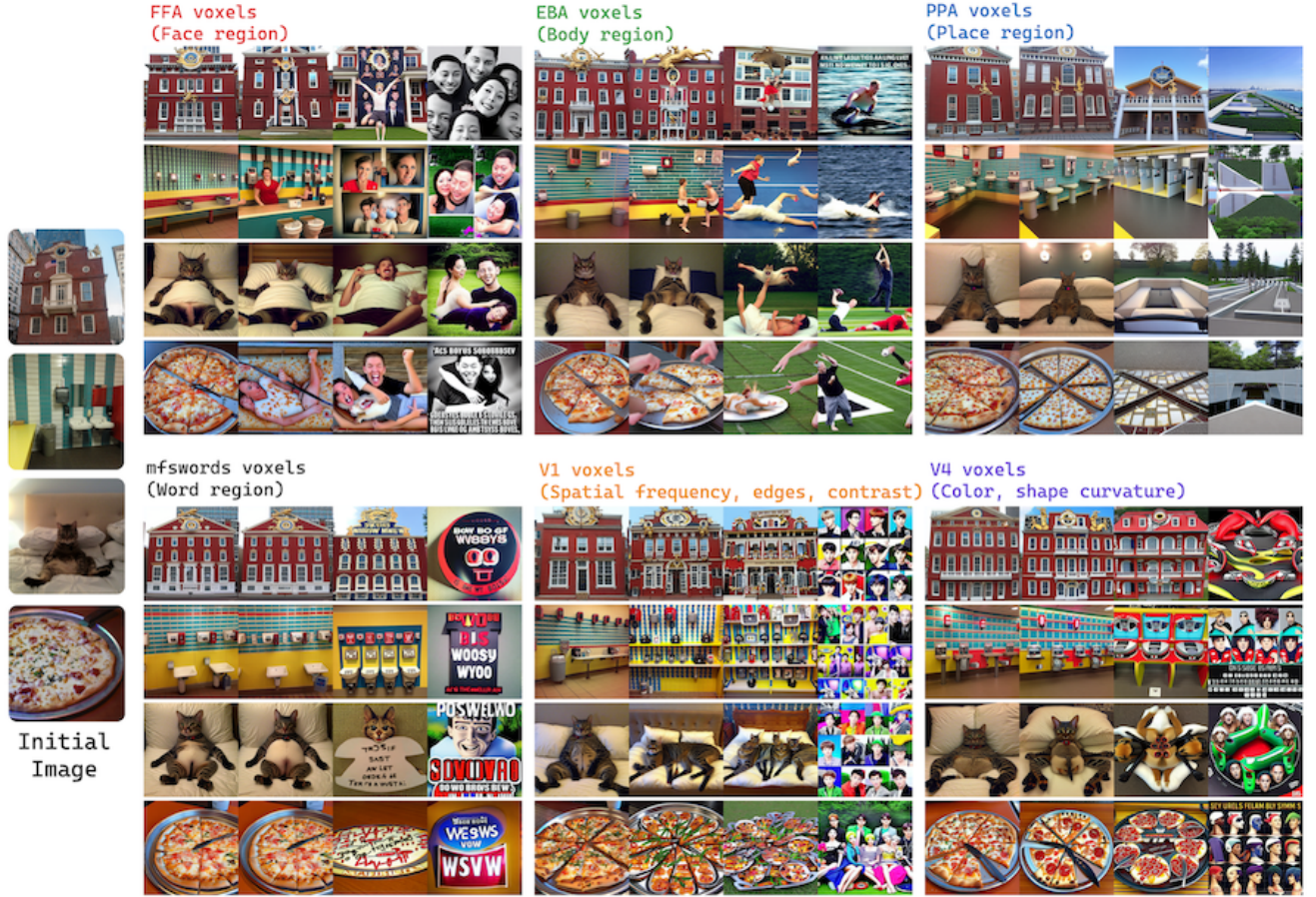


Figure S19. **Region-specific image evolution under neural objectives (S6).** Starting from the same seed images (left column), we optimize toward a neural objective of maximizing voxel activity in six distinct visual ROIs: FFA (faces), EBA (bodies), PPA (places), mfswords (words), V1 (edges/contrast), and V4 (color/curvature). For each ROI, we show the generated images at **20%, 50%, 80%, and 100%** progress along the optimization trajectory, illustrating how the visual representation gradually evolves as the embedding aligns with the target neural response.

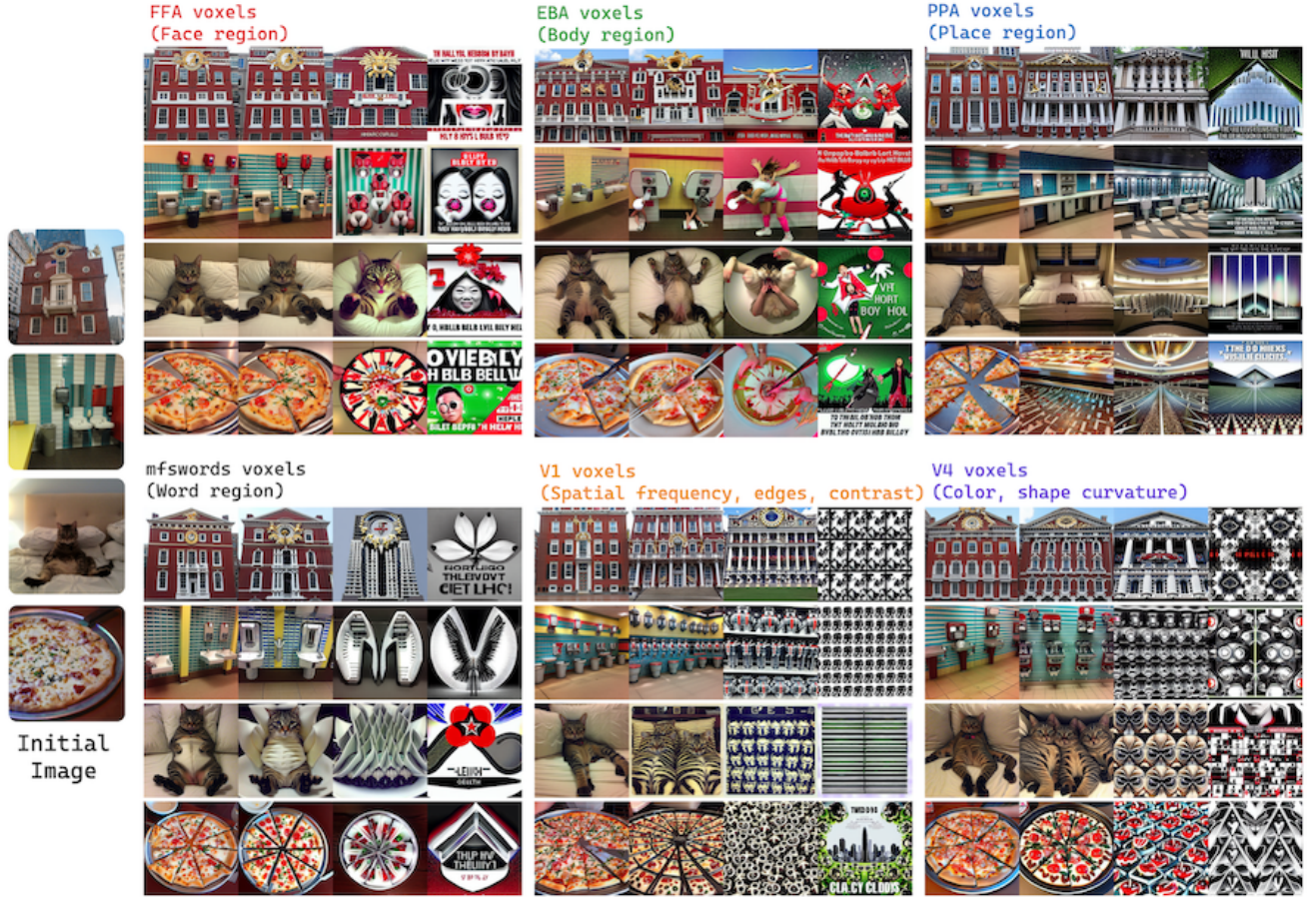


Figure S20. **Region-specific image evolution under neural objectives (S7).** Starting from the same seed images (left column), we optimize toward a neural objective of maximizing voxel activity in six distinct visual ROIs: FFA (faces), EBA (bodies), PPA (places), mfswords (words), V1 (edges/contrast), and V4 (color/curvature). For each ROI, we show the generated images at **20%, 50%, 80%, and 100%** progress along the optimization trajectory, illustrating how the visual representation gradually evolves as the embedding aligns with the target neural response.

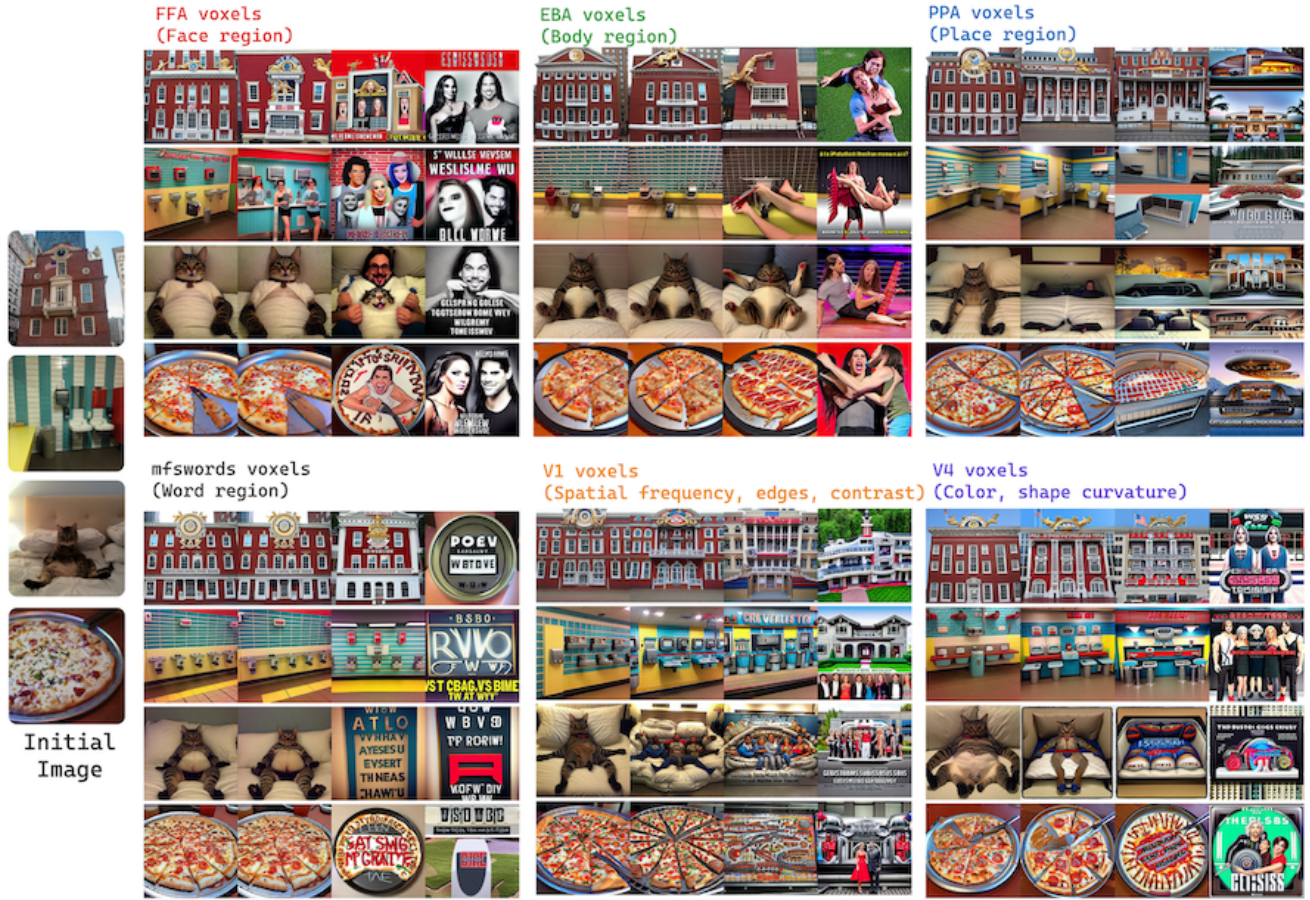


Figure S21. **Region-specific image evolution under neural objectives (S8).** Starting from the same seed images (left column), we optimize toward a neural objective of maximizing voxel activity in six distinct visual ROIs: FFA (faces), EBA (bodies), PPA (places), mfswords (words), V1 (edges/contrast), and V4 (color/curvature). For each ROI, we show the generated images at **20%, 50%, 80%, and 100%** progress along the optimization trajectory, illustrating how the visual representation gradually evolves as the embedding aligns with the target neural response.

A.5. Semantic classification setup and results

In this section, we provide additional results from the CLIP-based semantic classification analysis used to evaluate the semantic consistency of images generated from category-selective voxels. For each semantic category, we condition the optimization on maximizing responses in the place-, face-, word-, and body-selective voxels, and generate 1,000 NeuroVolve images using random natural images as initialization. We then apply a CLIP-based semantic probing procedure that classifies each generated image into one of four candidate categories. For each voxel set, we compute the proportion of generated images whose CLIP-predicted label matches the preferred category of that region. Across all ROIs, NeuroVolve consistently achieves higher semantic classification accuracy than (1) the *top-100 natural NSD images* ranked by mean true fMRI beta, and (2) the *top-100 BrainDiVE-generated images*, as reported in the BrainDiVE paper. These findings indicate that NeuroVolve exhibits substantially higher semantic specificity than both natural stimuli and prior generative baselines. (BrainScuba is not included, as comparable results are not reported.)

For all CLIP probes, we use **CoCa ViT-L/14**, and classify each image into four categories: *face*, *place*, *body*, *word*. We report the percentage of images for which the CLIP-predicted category matches the preferred category of the corresponding ROI. NeuroVolve images, evaluated using its own encoding model, consistently outperform both the natural-image top-100 set and the BrainDiVE top-100 set, demonstrating the model’s strong ability to synthesize semantically aligned, category-selective stimuli.

	Faces				Places				Bodies				Words			
	S1	S2	S3	S4	S1	S2	S3	S4	S1	S2	S3	S4	S1	S2	S3	S4
NSD top-100	40.0	45.0	38.0	41.0	68.0	78.0	81.0	72.0	49.0	59.0	60.0	49.0	30.0	48.0	30.0	25.0
BrainDiVE-100	69.5	68.0	67.0	71.0	97.5	100	100	100	75.5	69.0	59.0	72.0	60.0	61.0	61.0	34.0
NeuroVolve-100	72.0	100	71.0	99.0	100	100	100	100	44.0	54.0	87.0	97.0	99.0	95.0	100	16.0

Table S1. **Semantic specificity (S1–S4)**. Evaluating semantic specificity with zero-shot CLIP classification for S1 to S4.

	Faces				Places				Bodies				Words			
	S5	S6	S7	S8	S5	S6	S7	S8	S5	S6	S7	S8	S5	S6	S7	S8
NSD top-100	43.0	46.0	35.0	36.0	93.0	55.0	76.0	48.0	55.0	61.0	63.0	61.0	33.0	32.0	26.0	21.0
BrainDiVE-100	64.0	57.9	69.0	72.0	100	99	94.0	94.0	77.0	72.0	65.0	67.0	80.0	75.0	25.0	56.0
NeuroVolve-100	99.0	82.0	69.0	93.0	100	100	100	100	92.0	17.0	27.0	35.0	34.0	76.0	41.0	89.0

Table S2. **Semantic specificity (S5–S8)**. Evaluating semantic specificity with zero-shot CLIP classification for S5 to S8.

CLIP prompts Here we list the text prompts that are used to classify the images for Tab.1 and Tab.S1, Tab.S2.

Category	Prompts
Face	A face facing the camera; A photo of a face; A photo of a human face; A photo of faces; A photo of a person’s face; A person looking at the camera; People looking at the camera; A portrait of a person; A portrait photo
Body	A photo of a torso; A photo of torsos; A photo of limbs; A photo of bodies; A photo of a person; A photo of people
Place	A photo of a bedroom; A photo of an office; A photo of a hallway; A photo of a doorway; A photo of interior design; A photo of a building; A photo of a house; A photo of nature; A photo of landscape; A landscape photo; A photo of trees; A photo of grass
Text	A photo of words; A photo of glyphs; A photo of a glyph; A photo of text; A photo of numbers; A photo of a letter; A photo of letters; A photo of writing; A photo of text on an object

A.6. Activation Comparison of Final Generated Images

We further evaluated the distribution of NeuroVolve’s final generated images using an alternative visual encoder (CLIP ViT-H/14 with a single linear readout). Specifically, we retrained the voxelwise encoding model using this ViT-H/14 backbone and computed predicted responses for three image sets: (1) all NSD images viewed by the subject, (2) the top-100 NSD images ranked by the ViT-H/14-based encoder, and (3) the top-100 NeuroVolve-generated images, also ranked by the same encoder. Across all regions, NeuroVolve images consistently elicited substantially higher predicted activations than those evoked by natural stimuli. This indicates that NeuroVolve reliably synthesizes content that drives voxel responses beyond the range observed for real images, demonstrating its ability to generate strongly activating, functionally targeted stimuli.

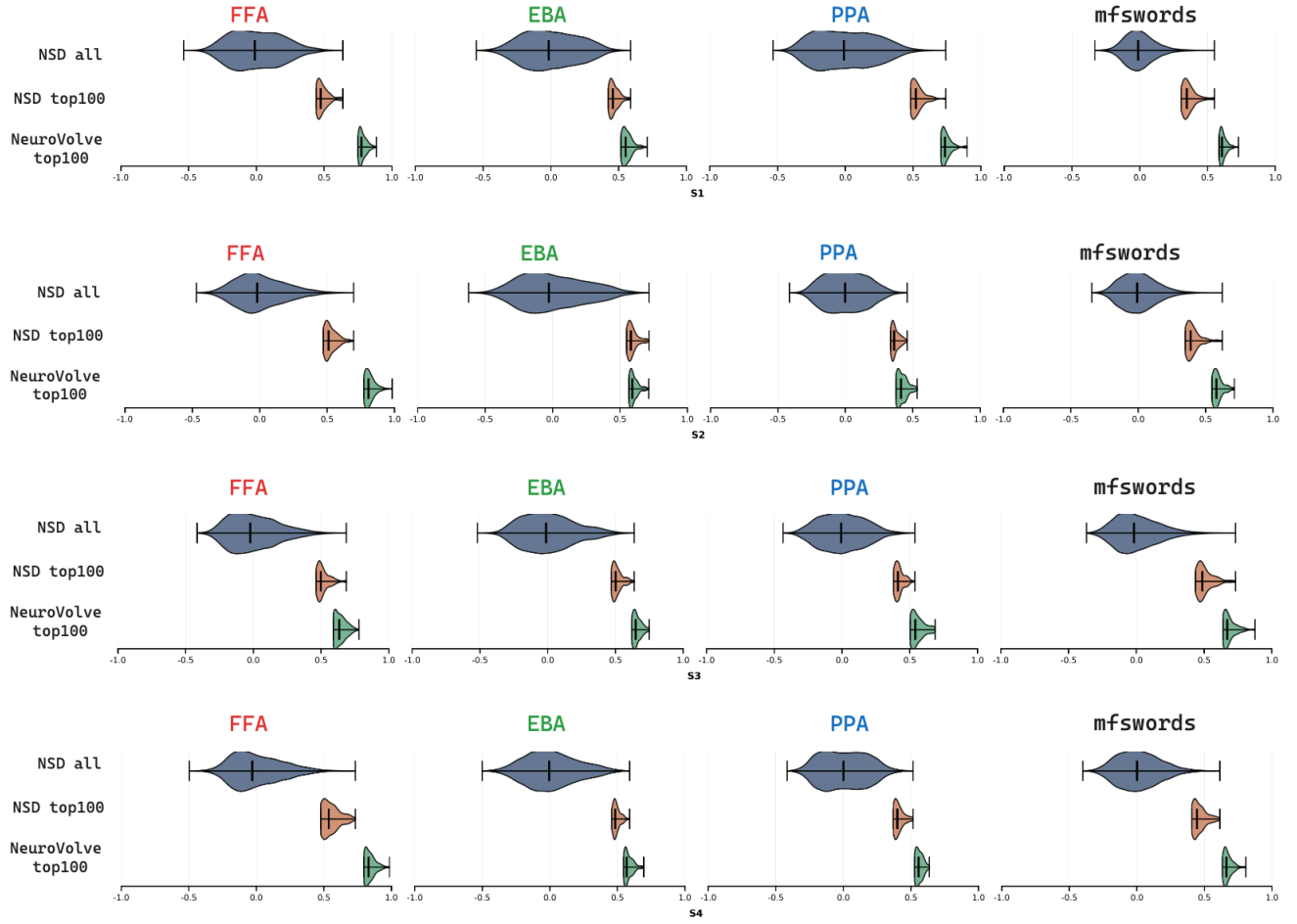


Figure S22. Predicted activation distribution of final images for S1-S4.

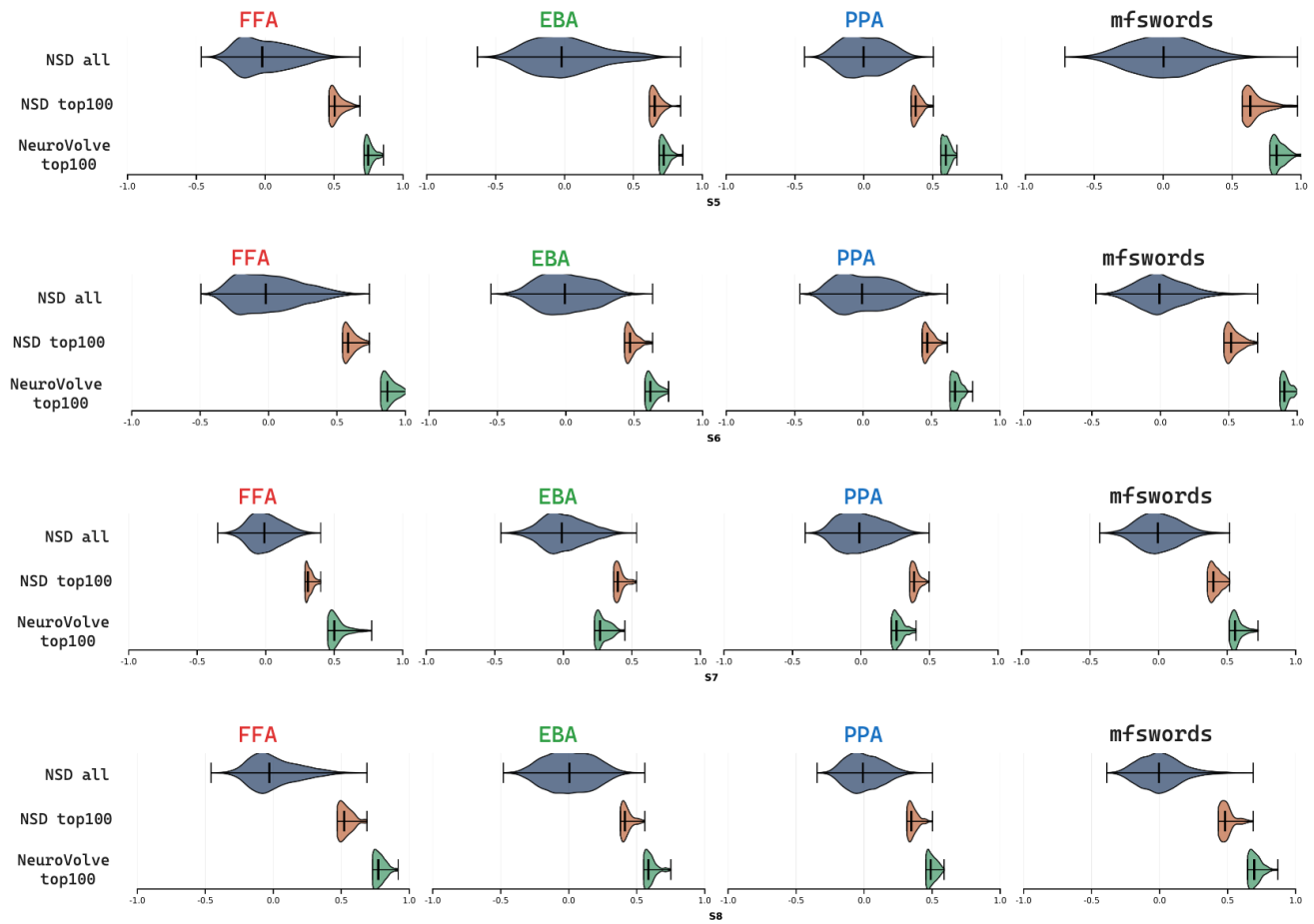


Figure S23. Predicted activation distribution of final images for S5-S8.

A.7. Optimization Trajectories

The optimization in BLIP Q-former embedding space is performed using the Adam optimizer with a learning rate of 0.01. Here, we visualize several additional optimization trajectories for different target regions and neuro objectives. In all cases, the optimization consistently increases the neural objective—i.e., it successfully maximizes the predicted activation of the selected voxel set. The curves are smooth and exhibit stable convergence, demonstrating that the NeuroVolve embedding-space optimization reliably reaches high-activation solutions.

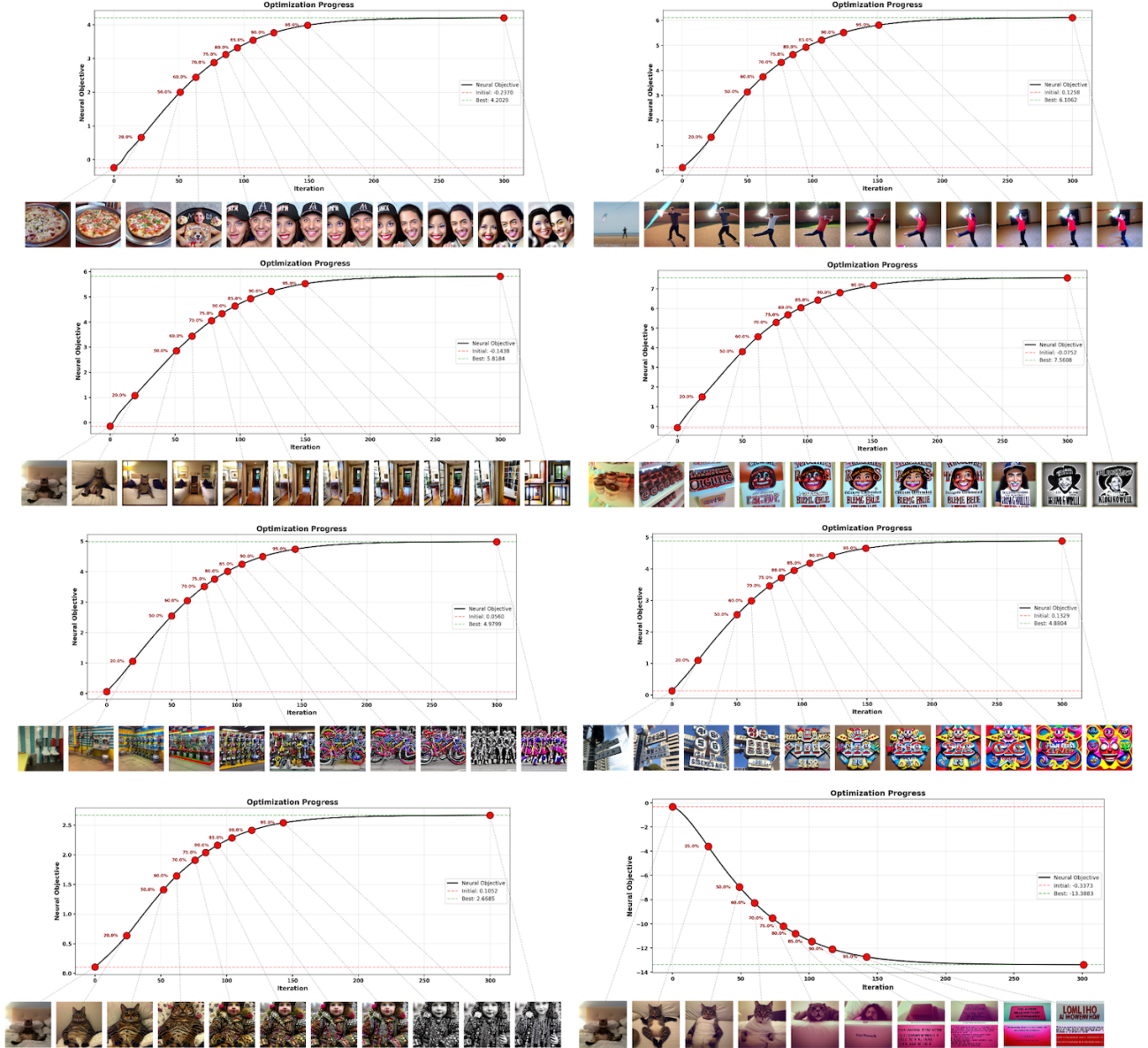


Figure S24. **Additional optimization trajectories in BLIP Q-former embedding space.** Each panel shows the optimization of the neural objective using Adam (learning rate 0.01), together with intermediate generated images. These results demonstrate the stability and robustness of the NeuroVolve optimization process in embedding space.